DIPLOMARBEIT

Aerosol measurements at the Sonnblick Observatory - analysis of elements and evaluations regarding the chemical composition

Aerosolmessungen am Sonnblick Observatorium - Elementanalytik und Auswertungen zur chemischen Zusammensetzung

Ausgeführt am Institut für
Chemische Technologien und
Analytik

der Technischen Universität Wien

unter der Anleitung von
ao.Univ.Prof. Dipl.-Ing. Dr.techn. Anne Kasper-Giebl

durch

Michaela Zuckerhut, BSc

Datum

Unterschrift (Student)

Abstract

Desert areas contribute significantly to the global aerosol load, with Saharan dust also reaching the Alpine region in Austria. The influx of minerals is of interest due to the associated impact on the radiation balance in glacier areas and also the nutrients included in the dust. The background station at the Sonnblick Observatory provides the necessary infrastructure and enables measurements unaffected by local emissions. The sampling of atmospheric aerosol (PM10, particles with aerodynamic diameter below and including 10 µm) is done on quartz fiber filters in a High Volume Sampler with weekly resolution. Aliquots of these filters are taken and subsequently digested with the aid of microwave irradiation. The solutions generated are analyzed by ICP-MS and ICP-OES for elemental identification and quantification.

Within this work, the analysis of eleven elements (Mg, Al, Ca, Ti, Cr, Mn, Fe, Co, Ni, Sr, Pb) was feasible. Sufficiently low limits of detections (LOD) could be reached for elements such as Fe, Al, and Pb while others proved to be more problematic with relatively high LODs, such as Mg and Sr. The results could be evaluated as temporal trends. We see that elevated concentrations mainly occur in the spring, summer and fall. Even more apparent is the correlation of elemental concentrations with Saharan dust events (SDEs). To explore this, five categories were defined, depending on how many days of the week were affected from Saharan dust, or how many days before or after the week a SDE occurred. We see that highest elemental concentrations of relevant elements such as Fe, Al and Ca coincide with the weeks that are most affected by mineral dust. Based on approximations taken from literature which aim to include additional mass factors such as oxygen and hydrogen, the mineral dust load could be calculated from the elemental concentrations. This estimates the mineral dust proportion of the total suspended particle mass concentration as up to 71% in weeks with relatively high Sahara dust occurrences.

The results allow an estimation of the contribution of long-range transport of mineral dust to the overall aerosol mass. Furthermore, the change in aerosol composition during SD occurrences in the region around Sonnblick Observatory can be described. Thus, the data provides the basis

to estimate effects on the ecosystem, such as the change of albedo and deglaciation affected by natural and anthropogenic particulate matter sources.

Kurzfassung

Wüstengebiete tragen wesentlich zur globalen Aerosolmenge bei, Saharastaub erreicht dabei auch das Alpengebiet in Österreich. Interessant ist der Eintrag des Mineralstaubs durch die verbundene Auswirkung auf die Strahlungsbilanz in Gletschergebieten und auch aufgrund des Nährstoffeintrags. Die Hintergrund-Station am Sonnblick Observatorium stellt die dazu benötigte Infrastruktur bereit und ermöglicht Messungen abseits von lokalen Emissionen. Die Probennahme des atmosphärischen Aerosols (PM10, Partikel mit aerodynamischen Durchmesser unter und einschließlich 10 µm) erfolgt auf Quarzfaserfiltern in einem High Volume Sammler. Die Zeitauflösung der Messungen liegt bei jeweils einer Woche. Aliquote dieser Filter werden entnommen und anschließend in der Mikrowelle aufgeschlossen. Die Lösungen daraus können mit ICP-MS und ICP-OES auf die enthaltenen Elemente analysiert werden.

Im Zuge dieser Arbeit war die Analyse von elf Elementen (Mg, Al, Ca, Ti, Cr, Mn, Fe, Co, Ni, Sr, Pb) möglich. Niedrige Nachweisgrenzen konnten für Elemente wie Fe, Al und Pb erreicht werden, während sich andere Elemente als problematischer herausstellten, wie zum Beispiel Mg and Sr. Die Ergebnisse konnten als zeitliche Verläufe ausgewertet werden. So kann beobachtet werden, dass erhöhte Konzentrationen vor allem im Frühling, Sommer und Herbst auftreten. Noch auffälliger sind die Korrelationen der elementaren Konzentrationen mit Saharastaub-Events. Um diese zu untersuchen, wurden fünf Kategorien erstellt, je nachdem wie viele Tage der Woche von Saharastaub betroffen waren, oder wie viele Tage die Woche von einem Saharastaub-Event entfernt ist. Wir beobachten, dass die höchsten elementaren Konzentrationen von relevanten Elementen wie Fe, Al und Ca mit den Wochen übereinstimmen, die am meisten von Mineralstaub betroffen sind. Mit geeigneten Formeln aus der Literatur, die darauf abzielen, zusätzliche Massen-Faktoren wie Sauerstoff und Wasserstoff zu inkludieren, konnte die Mineralstaubbelastung mit den elementaren Konzentrationen berechnet werden. Damit konnte der Mineralstaubanteil an absolut suspendierter Partikelkonzentrationen in Wochen mit relativ hohem Saharastaubaufkommen auf bis zu 71% geschätzt werden.

Die Ergebnisse erlauben eine Abschätzung des Beitrags des Ferntransports von Mineralstaub zur gesamten Aerosolmasse. Außerdem ermöglichen die Erkenntnisse, ein Bild von der Veränderung der Aerosolzusammensetzung während Saharastaubvorkommen in der Region um das Sonnblick-Observatorium zu zeichnen. Damit liefern sie die Grundlage für die Abschätzung von Auswirkungen auf das Ökosystem, wie z.B. die Veränderung der Albedo und die Abschmelzung der Gletscher durch natürliche und anthropogene Feinstaubquellen.

Acknowledgments

First and foremost I would like to thank Prof. Anne Kasper-Giebl very much for the opportunity to work on my thesis under her guidance; I appreciate all the advice and continuous support. Likewise the group, especially Bernadette, Daniela, Felix, Hong, Jakub and Karoline, were always there to make the work enjoyable and help with problems. I would like to thank Prof. Andreas Limbeck and his group for providing the opportunity to work on the ICP-MS and -OES, and sharing their expertise on it.

A special thank you is also extended to staff at the Sonnblick Observatory, for their reliable support when it comes to sampling, and to the colleagues from ZAMG for providing the modelling data.

I would like to thank Karoline Rieger for the supply of the ion chromatography results processed within this work. For the XRF measurements used within this thesis, my gratitude is owed to the X-ray center at TU Wien under the admission of Johannes Zbiral.

I also want to give a big thanks to all the friends sharing my way for longer or for shorter, in- and outside of university, for making this journey from a young high school graduate to now finishing my master's degree a fun adventure and wholesome experience. Gratitude is owed to my boyfriend Stephan as well, for being there whenever things did not seem so easy.

Last but not least I sincerely want to thank my family, especially my parents, for always believing in me and giving me the kind of support one should never take for granted. Thank you for your continuous encouragement in all fields of life.

Contents

Chapter 1

Introduction

1.1 Particulate matter

In the atmosphere surrounding our planet reside, besides gases, also airborne particles. They are either liquid, solid or a mixture of both and can influence the quality of the air we breathe. The term particulate matter (PM) is often narrowed to PM10, which includes all particles with an aerodynamic diameter of 10 µm or less; sometimes also PM2.5 (particles with an aerodynamic diameter of 2,5 µm or less) is reported. When estimating the impact of PM on human health, both the chemical composition and the size distribution of the particles have to be taken into consideration. While PM10 can reach the lower parts of the respiratory tract, PM2.5 can already enter the alveoli [1]. Because of the potential risks for the human body, reference and threshold values are set by various regulatory entities to protect the public. In table 1.1, the guideline value recommended by the world health organization (WHO) and the limit values of the European and the Austrian government for PM10 are listed.

Table 1.1: Limit and guideline values for PM10

Document	Yearly average	Daily average
WHO Air Quality Guidelines 2021 [2]	15 µg/m^3	45 µg/m^3 (with 3-4 exceedances per year)
Immissionsschutzgesetz Luft (IG-L) [3]	40 µg/m^3	50 µg/m^3 (with 25 exceedances per year)
Directive 2008/50/EC [4]	40 µg/m^3	50 µg/m^3 (with 35 exceedances per year)

In order to protect the public health and avoid implementation of ineffective regulations, the factors contributing to the PM load and toxicity, such as source and chemical composition, have to be characterized. Determining the contribution of natural source to PM is also interesting for countries and governments in the European Union. If the PM contribution is categorized as natural, it can be subtracted from the daily limit value exceedances of PM10 as per European Air Quality Directive (2008/50/EC) [4]. A distinction is made here between occasional types of natural contributions, such as Saharan dust and wildfires, and continuous sources of natural PM, such as sea spray [5].

1.1.1 Sources of PM

Sources of PM are varied and influence the size distribution and chemical composition of the particles. One can distinguish between anthropogenic vs. natural sources, primary vs. secondary particle formation and focused vs. diffuse sources. Primary particles are emitted directly from the source, whereas secondary particles are formed in the air by chemical reaction. The size range for secondary particles commonly lies in the submicron region, primary particles usually exceed a size of 1 µm aerodynamic diameter [1]. Possible sources of airborne PM include anthropogenic ones such as industrial activities, tyre and road wear or combustion processes, but also natural sources such as sea salt, dust, pollen, volcanic ash or wildfires [5, 6].

1.2 Mineral dust

A permanent and significant part of the natural PM in Earth's atmosphere and the most interesting fraction for this thesis is mineral dust (MD), which mainly originates in the large desert regions around the globe [7]. The biggest contributor to the mass of airborne MD is the Saharan desert, making up about half of the annual dust production [8]. The particles, which can be transported over large distances of up to several thousand kilometers, cause events of naturally elevated PM10, in Europe more frequently in the spring and summer months [5]. Data from the Western Alps suggests that because of drier climates during the winter in North Africa and more powerful winds (Atlantic southwesterlies) in the spring/summer time, dust transport from the region has increased after 1870 [9, 10, 11]. The influx of mineral particles themselves also has an influence on flora, fauna and on Earth's weather and climate. The dust particles can act as ice or cloud condensation nuclei but can also have an effect on the radiation budget of the globe by scattering and absorbing incoming or outgoing radiation [7]. Dust has biogeochemical impacts as a source of nutrients, with phosphorus being the most important factor on land and iron in marine ecosystems [12]. Soluble iron compounds stemming from Saharan dust act as a significant nutrient source in the Amazon rainforest, which is otherwise low in fertility [13]. As such, MD also contributes to changes in biological communities [14]. This is also hypothesized for the Alpine area, where Saharan dust affects terrestrial and aquatic ecosystems [15]. Dust in general also constitutes a large part of the soil in certain areas, such as regions where loess can be found [12].

1.2.1 Composition and source apportionment

When looking at the composition of mineral dust, different parameters can be investigated. Three important ones concerning the chemical composition are the elemental data, isotopic composition and mineralogical composition [7].

Considering the composition of dust of North Africa in terms of elemental abundance, silicon is the most abundant, followed by aluminium. Another major element is iron, with its compounds showing high absorption coefficients, making them relevant to the discussion of the radiative budget affecting the albedo. As mentioned before, iron as part of aeolian dust also has a strong influence as a nutrient in both marine and terrestrial ecosystems. Other elements worth mentioning early on in the description of composition are potassium, calcium, sodium, magnesium, titanium and phosphorus [16]. The elements mentioned (except phosphorus) have also been subject to various source discrimination studies considering different elemental ratios [16, 17, 18]. Typically, aluminium is used as the reference element and compared against the mentioned elements in these source apportionment endeavors.

Regarding the mineralogical phases present in mineral dust, silicon is usually present in the form of its oxides in various kinds such as quartz [7]. Aluminium often occurs as a combination with the earlier mentioned silicon in alumosilicates, such as feldspar. For calcium and magnesium, calcite and dolomite are relevant minerals. Neither the direct amount of quartz or feldspar, nor the comparison of both seem to indicate the origin of a dust sample, while the calcite and dolomite abundance can give more information on this matter [16, 19]. For example, African dust samples rich in carbonates, reaching more than 50%, point to an origin in the north west of North Africa. Determining the abundance of different clay minerals is also a possible method for determining the origin of the dust. Their amount in samples can range from trace levels to more than 60% in weight, with illite, kaolin and smectite group being the major constituents. The high variability of these components suggests that not only the origin location, but also transport parameters such as wind, speed and distance travelled affect the clay content. Besides these, various other minor types can occur, such as chlorite or white mica. The analysis for mineralogical composition is usually followed through with X-ray diffraction (XRD) measurements, which has been done for over 40 years. Because of the requirement for a relatively large amount of sample mass, XRD is mostly used for source sediments or prolonged exposure samples [7].

Another useful tool for source apportionment is isotopic data, especially of the elements strontium and neodymium [7]. Hafnium is another element that has been investigated in this context and provides information on origin [20].

1.2.2 Effects on climate and weather

High dust concentrations in the air can significantly affect the climate on the surface below [21]. Due to their bigger size and their tendency to be present in the troposphere, the particles not only seem to contribute to solar (short-wave) radiative forcing, but also thermal infrared radiative forcing [22]. Dust acts as a scattering particle in the short-wave range, while the longer waves emitted by Earth's surface are absorbed and afterwards re-emitted as thermal energy in no particular direction, also back to the surface. One cannot easily predict whether a population of particles will generally have a cooling or a heating influence on the climate. For the quantification of these effects, several properties of the dust such as the shape, size and composition, need to be considered and expressed as a function of wavelength. The impact of the dust is also dependent on its elevation in the air and on the nature of the surface beneath [23, 24].

1.3 Measurement location - Sonnblick Observatory

The Sonnblick Observatory (SBO) is located on the summit of the Hoher Sonnblick in the Austrian Alps, at an elevation of 3106 m above sea level, coordinates of 12°57' east longitude and 47°03' north latitude. The observatory is powered by electricity only and lies far away from densely populated or industrialized areas, thus, making it an ideal location for chemical background measurements [25]. The station can only be reached by cable car used for the transportation of observatory supplies and staff, or a five hour hike starting in the valley. Air from inside the observatory flows through a separate 20 m meteorological tower, as to not disturb measurements [26]. The mountain peak area is marked by glacier fields and surpasses the tree line by approximately 1000 m [27]. The facility was established in 1886 by meteorologist and ZAMG (Central Institution for Meteorology and Geodynamics) director Julius Hann and the mine owner Ignaz Rojacher, and has been expanded and developed over time. Today, there is a wide variety of over 50 measuring instruments available for the recording of different variables [28]. The Sonnblick Observatory is also part of the Global Atmosphere Watch Program (GAW) by the World Meteorological Organization (WMO). When investigating (Saharan) mineral dust, SBO offers a favorable location, since small-grained dust is usually lifted to high elevations [29]. In this thesis, particulate matter collected at SBO on quartz fiber filters by a High Volume Sampler was processed and then analyzed.

1.4 Task formulation

Quartz fiber filters sampled at the SBO in Austria in the years 2019-2021 had to be analyzed for the main components in mineral dust. For this purpose, they had to be digested and the acidic solutions were subsequently measured via analytical methods, i.e., inductively coupled plasma - mass spectrometry (ICP-MS) and optical emission spectroscopy (ICP-OES). For this purpose, a reliable method had to be developed with regard to the digestion process. The three annual cycles of concentration data were evaluated regarding their chemical composition and in the context of the occurence of Saharan dust events (SDE) predicted by model data provided by ZAMG. This permits further understanding of mineral dust in the background concentration of particulate matter in Austria.

Chapter 2

Methods and procedure

2.1 Sampling process

The air tight metal filter holders for the Digitel sampler are washed and cleaned at the TU Vienna before being loaded with the quartz fiber filters (Pallflex Tissuquartz-2500QAT-UP, size 150 mm) and transported to the High Volume Sampler (Digitel) at the SBO (fig. 2.1b), with the inlet on the roof of the observatory (fig. 2.1a). Each filter is sampled for one week with an average air volume of 3360 m^3 at standard conditions (273 K, 1013 bar), after which the filter is exchanged with a new one. Field blanks for result correction were also produced regularly, namely after every fourth regular sample filter. This was done by putting a new filter into the High Volume Sampler, sampling for approximately one minute, and then removing the filter. Within this work, filters from the years 2019 - 2021 were processed.

(a) Sampler inlet on top of the observatory (b) High volume sampler by Digitel

Figure 2.1: Sampling set-up at the Sonnblick Observatory, pictures taken by author

Volumes of air drawn through the sampling systems were automatically recorded in log files. When this was not possible because of problems with the automatic recording, manually noted start and end times were used for calculations of the air volumes. The volumes were corrected for standard conditions before usage for calculations.

The mass concentration of total suspended particles (TSP) is measured via β-attenuation (SHARP-Monitor Model 5030, Thermo Scientific) at the SBO, downstream a heated whole air inlet to counteract temperature and humidity influences in the high alpine setting. For the determination of PM via β-attenuation, the instrument is equipped with a radiation source and a detector that records the attenuation of the β-rays by the particles collected onto a filter tape [30]. Values derived from these measurements can be compared to PM10 concentrations as a first approximation, since at the high alpine site, particles with a diameter above 10 µm are unlikely to occur [27]. Values are recorded as 30-min averages in the unit of $\mu g/m^3$ and corrected for standard conditions (273 K, 1013 mbar).

Following the sampling period, filters are stored again in the metal filter holder and then transported to TU Wien. At the university, the filters are packaged to be stored long-term. The majority of filters processed in this thesis had been stored in plastic bags in the freezer. Starting with the filter from 17.06. to 24.06. 2021 (filter no. 280), a 47 mm diameter sample punch of each filter was also collected for analysis of microplastics and stored in an aluminium foil pouch. The remaining portion of the filter is again stored in a plastic bag in the freezer.

2.2 Instruments

2.2.1 Microwave

Digestion of solid matrices using acids and a microwave can significantly reduce the time required for the sample preparation, while also allowing for process automation. The frequency used by such instruments on the market is specified to be 2,45 GHz [31]. For this thesis, the Anton Paar Multiwave 5000 was used. The use of a closed-vessel system, as the one employed in the microwave, offers the possibility of reaching higher digestion temperatures, as they are not limited by the boiling temperature of the acid. At the same time, adhering to green chemistry principles, lower reagent volume can be used while the digestion efficiency is maintained [32]. Ten vessels manufactured from polytetrafluoroethylene (PTFE) were employed for the digestion. The ability to closely control digestion conditions in commercial microwave systems additionally enables reproducibility in the settings, and also allows the comparison of results between instruments. These methods of digestion with the aid of microwaves has been adapted by official authorities like the United States Environmental Protection Agency (EPA) [32]. The maximum temperature reached in our digestions is around 180-190 °C. In fig. 2.2, an example of a temperature program of a digestion run with ten filled vessels can be seen.

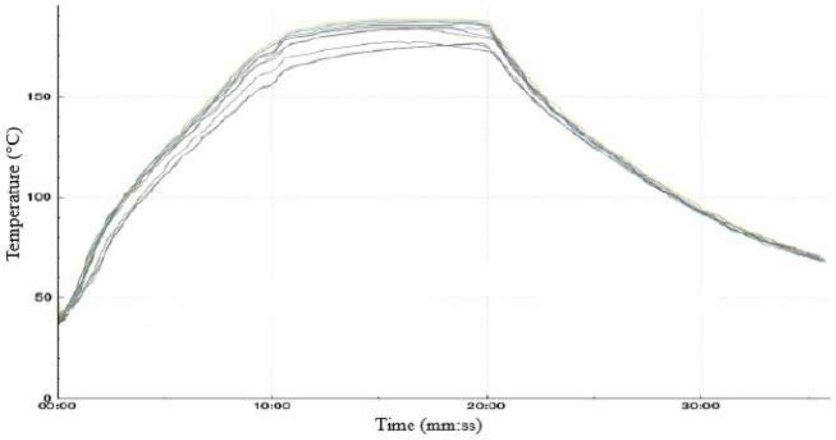

Figure 2.2: Plot of microwave program, each line describing one vessel

2.2.2 Inductively coupled plasma mass spectrometry (ICP-MS)

A quadrupole ICP-MS iCAP Qc (ThermoFisher Scientific, Bremen, Germany) was used for elemental quantification. ICP-MS offers a lot of advantages when considering its usage for environmental samples. Especially its low detection limits and high linearity are appreciated, and combined with its high throughput, it presents a fast and reliable method for analyzing elemental compositions [31]. When conducting analysis, the prepared sample, after vaporization, passes three parts of the instrument [33]. In the ion source, argon gas is ionized in a high-frequency field generating plasma, which is, in turn, able to ionize the sample molecules, which have been dispersed into an aerosol before reaching the gas flow [31]. In the following mass spectrometer, the generated ions are separated based on their mass-to-charge ratio [33]. The instrument used within this thesis is equipped with a quadrupole filter. These filters are set up by four parallel conducting rods with a cylindrical or hyperbolic shape. By adjusting the voltage applied to the rods, the mass-to-charge ratio of the ions that are able to pass is set. This parameter can be adjusted relatively quickly to ensure a fast and complete analysis. Finally, the ions need to be detected by converting them into an electrical signal [33]. To reduce the influence from polyatomic interferences, a collision cell for kinetic energy discrimination (KED) was used. Polyatomic ions are slower than atomic ions and also lose more kinetic energy when colliding with non-reactive gase molecules, thus making it possible to distinguish the two [34]. A mix of 7% H_2 in He is used in the collision cell. The parameters presented in table 2.1 were used for ICP-MS analysis within this thesis. As the measurement software and for evaluations afterwards, Qtegra was used.

Table 2.1: Parameters for ICP-MS measurements

Parameter	Setting
Nebulizer flow (l/min)	1,0464
Extraction lens voltage (V)	-101,7
Plasma power (W)	1550,0
Cool gas flow (l/min)	14,000
Auxiliary gas flow (l/min)	0,8000
CCT (collision cell technology) focus lens voltage (V)	-2,10
Collision gas flow (ml/min)	4,500
Pole bias (V)	-18,000
CCT bias (V)	-21,00

2.2.3 Inductively coupled plasma optical emission spectrometry (ICP-OES)

ICP-OES is another important analytical method in the field of environmental multi-element analysis. Here the goal is to measure the emission of characteristic radiation of the atoms excited by the plasma [31]. A Thermo iCAP 6500 ICP-OES instrument (ThermoFisher Scientific, Bremen, Germany) was used combined with an echelle optics and a charge injection device (CID) solid state detector. The digested sample is introduced into the instrument in liquid form via a Mira Mist nebulizer made out of polyether ether ketone (PEEK). Parameters for ICP-OES measurements are presented in table 2.2.

Table 2.2: Parameters for ICP-OES measurements

Parameter	Setting
Plasma power (W)	1300
Radial observation height (mm)	12,00
Monitoring time (s)	30
Data point collection interval (s)	0,5
Make-up gas flow of Argon (l/min)	0,25
Auxiliary gas flow (l/min)	0,8
Coolant gas flow (l/min)	14

2.3 Sample preparation and chemical analysis

For elemental analysis, eight circular sample punches with a diameter of 10 mm were used as an aliquot from both filter types (samples and field blanks) for digestion using the microwave. A glass punching tool was used and a teflon pad was placed underneath the filter as to avoid metal contamination. The filters to be sampled were taken out of their storage bag one by one and then punched on the cleaned teflon pad. The sample punches were kept in close-able petri-dishes until digestion. For digestion, the teflon vessels were filled with the punches and digestion liquids, except one vessel. This was only filled with the liquids and after digestion be stored as a kind of blank, which could give information about possible contamination in acids, vessels and processes used during sample preparation.

Different acid mixtures were evaluated for the digestion of the quartz fiber filter samples within this work, to ensure the best dissolution of both the filter and the collected matter. Hydrochloric acid (HCl, 37% for analysis, Merck KGaA, Germany), hydrofluoric acid (HF, 30%, Merck KGaA), nitric acid (HNO_3, 65% for analysis, Merck KGaA) and tetrafluoroboric acid (HBF_4, Apollo Scientific,UK, 50%, also ChemLab, Belgium, 38% ultra pure) were used. Even though HF is commonly used as a digestion agent in similar investigations, HBF_4 is a potential alternative that provides a safer source of fluoride ions, while maintaining the strong reactive capacity necessary for silicate digestion and avoiding formation of excess fluorides [35, 36]. The different compositions tested are presented in table 2.3. After digestion, the teflon vessels were removed from the microwave, opened, the liquid transferred to a sample vial (Cellstar® polypropylene centrifuge tubes 15 ml, Greiner, Austria) and the teflon vessel was rinsed three times to ensure quantitative transferal. As for the dissolution of the filters during the digestion, one could observe that the aqua regia mixture did not dissolve the filter in any visible way, the HBF_4 mixture showed very fine residues of filter material, while the HF mixture dissolved any existing filter material completely. The obtained liquid sample was weighed and then stored in the freezer until dilution and analysis.

Table 2.3: Composition of digestion mixtures

Digestion Mixture No.	HNO_3 (ml)	HCl (ml)	HF (ml)	HBF_4 (ml)	H_2O (ml)
1 (Aqua regia)	2	4	-	-	-
2 (HF mixture)	3	1	0,5	-	-
3 (HBF_4 mixture) [35]	3	-	-	1	2

To evaluate the correctness and accuracy of the results obtained by these different methods, the certified reference material (CRM) San Joaquin Soil (2709, NIST, USA) was also subjected to digestion. For this, eight blank punches obtained from new filters were digested with about 15 mg of the reference material.

Prior to analysis, the digested sample had to be further diluted with high purity water (resistivity 18,2 M*cm^{-1}, treated with Milli-Q Reference by Millipore). In this work, the samples were volumetrically diluted by a factor of 100 prior to ICP-MS measurements, but the actual dilution factor of each sample was determined gravimetrically. For the ICP-OES samples, this factor was reduced to 10 because of the instrument's higher tolerance for fluoride ions potentially produced by the HBF_4 and the higher detection limit of the ICP-OES. Besides the sample dilutions, a standard series for quantification by external calibration and blanks were prepared. The standard solutions used for ICP-MS ranged from 0,1 to 10 µg/kg, for ICP-OES standards with concentrations from 0,05 to 5 mg/kg were employed. These calibration ranges are usually used for the instruments, and could be applied for the samples. Certified reference materials were used for the preparation of standards (ICP standard stock solutions multi-element VIII and Ti from Merck KGaA, Certipur© Certified).

Because of fluctuation in parameters such as plasma strength and gas flow, the performance of an ICP-MS unit can vary within a measurement series. To monitor the analysis and assess recovery during measurements, indium (taken and diluted from In standard stock solution from Sigma Aldrich, Certipur© Certified) was added to all ICP-MS analysis solutions.

2.4 Ion chromatography

For additional information apart from elemental analysis, results gathered by ion chromatography were used within this thesis. The analysis was done by members of the research group. Ions are separated via an ion-exchange column based on their charge and size. In table 2.4, the used system is described.

Table 2.4: Ion chromatography parameters

	Cations	Anions
Instrument	Dionex Aquion	Dionex ICS 1100
Column	Dionex Ion Pac CS16	Dionex Ion Pac AS22
Pre-column	Dionex Ion Pac CG16	Dionex Ion Pac AG22
Eluent	30 mM MSA	4,5 mM Na_2CO_3 / 1,4 mM $NaHCO_3$
Flow	1 ml/min	1 ml/min
Suppressor	Dionex CDRS 600 - 4 mm (electro-chemical)	Dionex AERS 500 - 4 mm (electro-chemical)
Regenerant	Eluent in recycle mode	Eluent in recycle mode
Sample loop	150 µl	150 µl
Detection	Conductivity detection	Conductivity detection
Software	Chromeleon 7.10	Chromeleon 7.10

2.5 X-ray fluorescence (XRF) measurements of mineral dust deposits

To obtain a larger amount of mineral dust, three snow samples were collected from the roof of the SBO in March of 2022. During that time period, an intense transport event of Saharan dust occurred in Austria. A 50x50 cm area of snow with a depth of approximately 13 cm was sampled. For the preparation of XRF samples, the snow samples were thawed, the liquid collected with a pipette, and the residue dust was dried on a heating plate at around 130 °C. The supernatant liquid was weighed and filtrated onto quartz fiber filters, with the aid of vacuum suction. Here one could observe that while the majority of the dust sedimented at the bottom of the thawing containers, some material stayed suspended. Gravimetric data for this is provided in table 2.5. As we can conclude from the percentage of suspended matter, only a small amount of the mineral dust at SBO falls into this category. Because of this, we can state that the sedimented dust is representative for the overall material we collected on the filters.

Table 2.5: Gravimetric analysis of mineral dust deposits

Date	Sedimented Dust (g)	Suspended Dust (mg)	Percentage Suspended (%)	Snow (g)	mg Dust/g Snow
16.03.2022	0,121	2,4	1,9	176	0,17
20.03.2022	0,435	12	2,6	654	0,68
22.03.2022	0,0902	0,41	0,46	522	1,2
27.03.2022	0,929	2,5	0,27	782	0,70

Resulting dry samples were then subjected to XRF analysis, conducted at the X-ray center at TU Wien. First, 6.5 g di-lithium tetraborate and 0.7 g sample were weighed into a platinum crucible and melted at 1000 °C in air. The holding time at 1000 °C was 30 minutes, until transparency is reached. The melted mixture was then poured into a platinum mold heated to 300 °C to form a fused tablet. The analysis of the tablet was performed using an Axios Advanced wavelength dispersive X-ray fluorescence spectrometer (Malvern Panalytical, UK) with a rhodium front window tube. The excitation voltage used was 50 kV with a tube current of 50 mA. The measurements were performed under vacuum. For the evaluation of the measured element intensities, standards from the company Malvern Panalytical (UK) were used.

Chapter 3

Results and discussion

Of all the filters collected between 2019 and 2021 (17.1.2019 - 16.12.2021), 174 were digested (141 sample filters, 33 blank filters). Some filters could not be processed due to problems during sampling, resulting in wetness and disposal. For other weeks no filters were available due to malfunctioning of the High Volume Sampler (22.9. - 5.11.2020). Analysis by ICP-MS was done on all 174 of the received digestion solutions. To test ICP-OES as a potential future alternative to ICP-MS, analysis was performed for 30 of the sample filters and 2 of the blank filters using ICP-OES.

3.1 Method development

3.1.1 Comparison of different digestion methods

Prior to the digestion of the sample filters from SBO, the different digestion methods presented in table 2.3 using a variety of acids were evaluated on basis of their achieved recovery of the elements in focus when using certified reference material (CRM). For a detailed description of the practical execution of this step, see section 2.3. For this evaluation of different acid mixtures, around 15 mg of CRM were digested, six times for each mixture. Eight 10 mm punches of new quartz fiber filters were added in each digestion vessel to account for a possible matrix effect. Measurement results obtained by ICP-MS were reported as parts per billion (ppb, equivalent to µg/kg) calculated on a mass basis. These mixing ratios were then converted into mg/kg CRM sample using formula 3.1. The mass of the "Digested Sample" here refers to the amount of liquid transferred from the teflon vessel into the sample vial for further dilution and analysis after microwave digestion. The dilution factor was approximately 100, the exact factor was determined gravimetrically for each sample.

$$\text{Concentration}(mg/kg) = \frac{\text{Concentration}(ppb) * \text{Dilution Factor} * \text{Digested Sample}(g)}{\text{Weighted CRM Sample}(mg) * 1000} \tag{3.1}$$

These results could then be directly compared to the given values of the CRM. This comparison is visualized in figure 3.1 and the recoveries in percentage of the given CRM value can be seen in table 3.1. Recoveries highlighted in green represent the best result achieved for the single elements. This classification already indicates that the method using HBF_4 might become the method of choice. Of the twelve elements considered, eight displayed average recoveries ranging from 89 - 107% when utilizing the HBF_4 method. A higher deviation from the reference value was observed for elements calcium and potassium. Ca, just like Mg, is an indicator for the occurrence of mineral dust [37]. Thus, an accurate determination would be desirable. Therefore, Ca was still included in the list of elements analysed by ICP-MS in the following steps, even though the recovery during this evaluation is less than ideal, possibly due to isotopic interferences. In parallel, a method for correction of the poor recoveries was worked on, which is discussed in section 3.1.4. K was not included in subsequent ICP-MS analysis, since calibration curves within this evaluation showed no reliable slopes. Results for K could be supplied by IC measurements. Values and quality of analysis of elements measured with ICP-MS were also compared to available ion chromatography (IC) results and ICP-OES measurements.

Table 3.1: Recoveries and standard deviations (SD) of various elements in %, with the closest result to 100% highlighted in green for every element

	Aqua regia	SD	Hydrofluoric acid	SD	Tetrafluoroboric acid	SD
24Mg	82	18	20	12	94	14
27Al	50	11	32	7	100	17
39K	14	5	48	10	69	3
44Ca	17	4	15	4	20	3
48Ti	72	19	74	8	85	15
52Cr	65	17	108	18	95	14
55Mn	86	21	100	14	97	16
56Fe	90	19	108	31	104	17
59Co	99	23	116	15	95	17
61Ni	89	22	119	21	107	20
88Sr	43	11	87	13	89	14
208Pb	61	9	76	17	85	16

Figure 3.1 again presents the recoveries, but adds information about the standard deviation of the results of the replicate analyses.

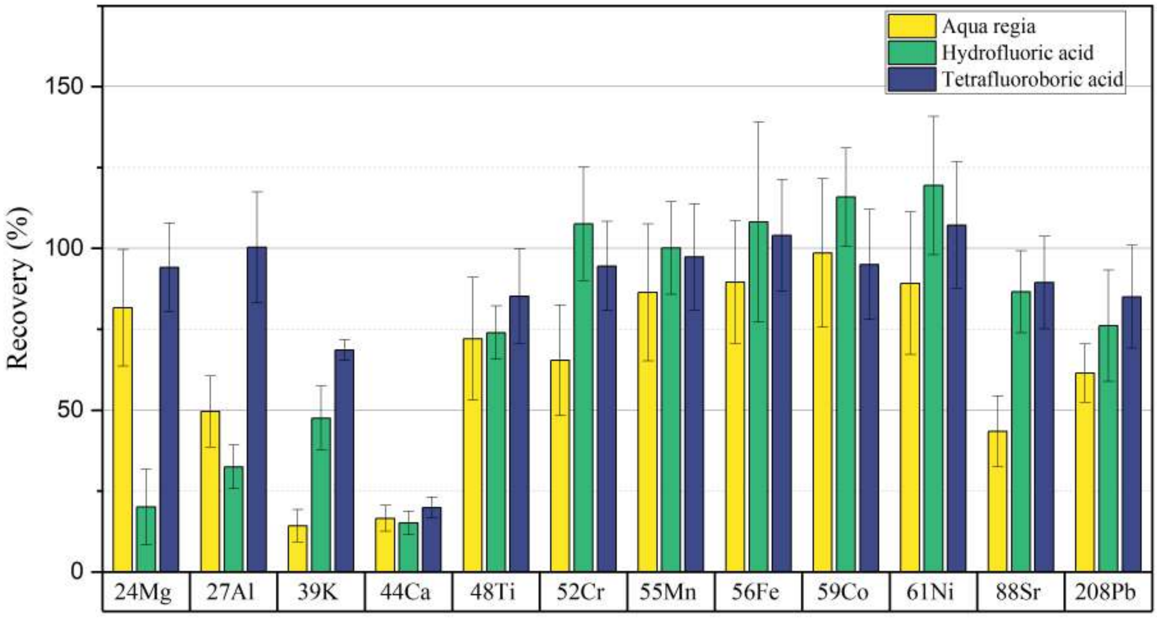

Figure 3.1: Recovery of chosen elements with different digestion methods, standard deviations also shown

With these results in mind, filters from SBO were digested using the HBF_4 method. The maximum standard deviation for all samples lies within a 20% margin for the HBF_4 method. The reproducibility of a measurement could be progressively improved still in the course of this diploma work, but CRM measurements were not repeated because of time pressure.

3.1.2 Use of Indium as internal standard

As explained in section 2.4, indium was added to all samples to be measured with ICP-MS to correct for possible drift phenomena, especially during longer measurement series. Since the In addition was recorded gravimetrically, mass correction of the signals was attempted and performed in all but one measurement series. For one series the mass correction led to more variation of the In signals, most possibly due to an error of the analytical balance. Knowing this, mass correction was only applied when a stabilization in In signals could be achieved. Ideally, the first sample would give a starting point all measurements of this series would be related to. However, correction was executed with a number of selected signals in the beginning, in order to achieve the most effective stabilization of the In signals in the respective measurement series.

3.1.3 Comparability of ICP-MS to ICP-OES results

Because the HBF_4 used in the digestion puts a strain on the ICP-MS instrument, ICP-OES measurements were considered as an alternative measurement method. To check the performance and the comparability to ICP-MS, the extracts of the digested CRM described in section 3.1.1 were also analyzed by ICP-OES. The results are compared in fig. 3.2.

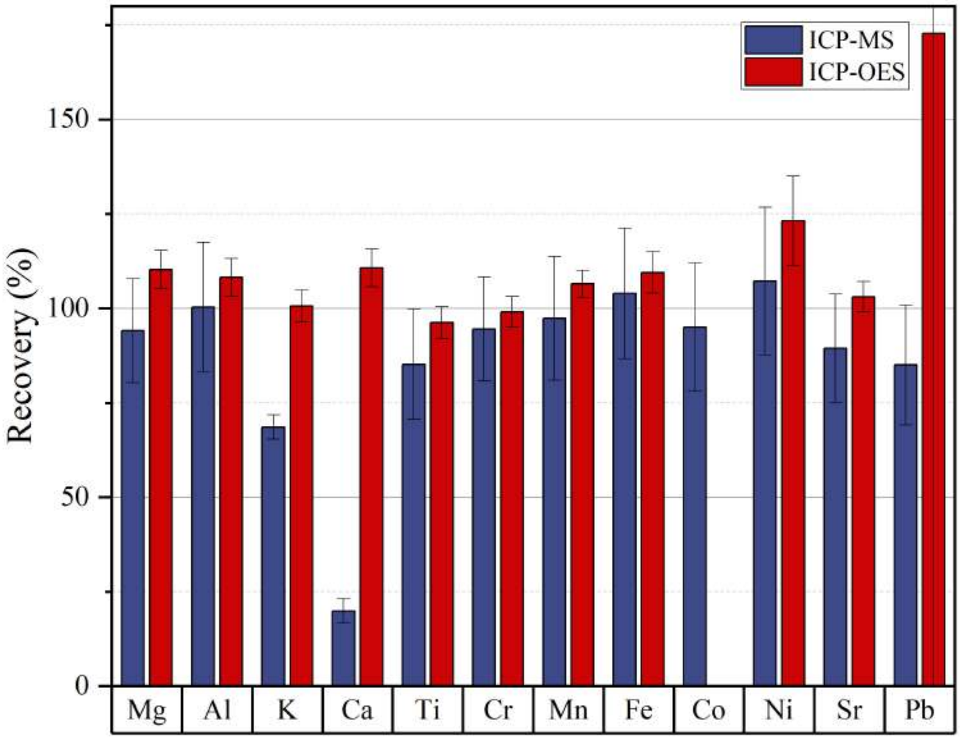

Figure 3.2: Comparison of recoveries in ICP-MS vs. ICP-OES

As is observable, for several elements of interest, such as Al and Fe, but also Ti, Cr, and Mn, ICP-OES is comparable to what is achievable with ICP-MS measurement. Strikingly different results were obtained for Ca and K, where the ICP-OES results show recoveries substantially closer to the target value. ICP-MS results for these two elements were repeatedly below expectations, and ICP-OES shows a more promising starting point for further analysis. Other elements show problems during ICP-OES analysis, for example Co only produces negative recoveries, while Pb is overestimated by more than 50%.

To further evaluate the comparability of the two analytical methods, a set of digested filter samples was analyzed by ICP-OES. In order to shine light on how the loading of the filters affected the comparison, the samples were chosen based on their range of Al and Fe concentration values obtained by ICP-MS. In the following, ICP-MS and ICP-OES comparisons are elaborated. Both ICP-MS and ICP-OES values in this case were not blank corrected, because the same extracts were used. When evaluating the results, we can see a similar picture as obtained for the CRM. In fig. 3.3, the ICP-MS/ICP-OES comparisons for the most promising and also important elements are illustrated. Fe (fig. 3.3a) and Al (fig. 3.3b) show a good agreement of both methods. Ca consistently shows higher concentrations when analysed by ICP-OES, which was also observed for the CRM (fig. 3.4). The results are discussed in detail in section 3.1.4. After removing an outlier, Mg concentrations show a high correlation, however, a relatively large offset can be observed for ICP-OES (fig. 3.3c). For Mn, also one of the values was classified as an outlier and removed, after which the compared values showed some correlation, with a slight offset (fig. 3.3d). Ti offers a good correlation, however ICP-MS values have a tendency to exceed ICP-OES findings (fig. 3.3e).

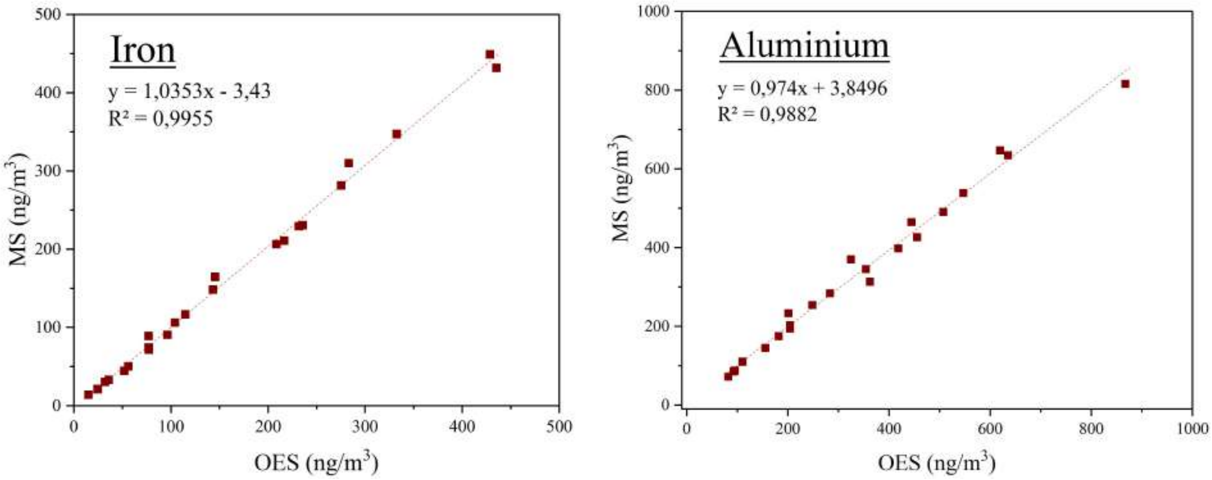

(a) Iron comparison (b) Aluminium comparison

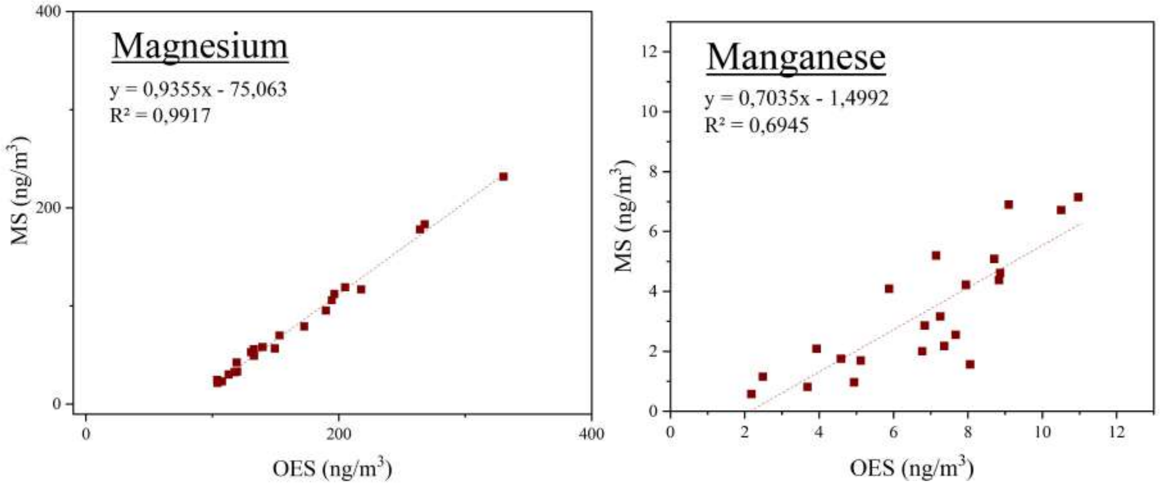

(c) Magnesium comparison (d) Manganese comparison

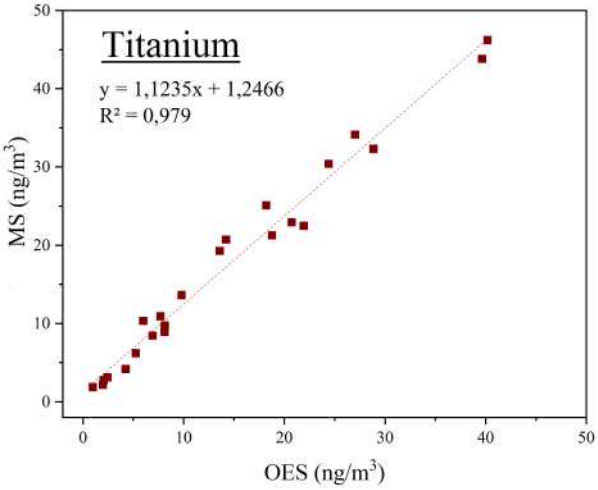

(e) Titanium comparison

Figure 3.3: Comparison of concentration data for filter measurements obtained by ICP-MS vs. ICP-OES analysis

3.1.4 Intercomparison for calcium

As mentioned earlier, ICP-OES results for Ca of the CRM showed a vastly better recovery rate than the corresponding ICP-MS results. Thus, further investigations how ICP-MS results could be improved will be described here. In fig. 3.4, we can see a direct intercomparison of results of filter measurements similar to those in fig. 3.3, also depicting the ICP-OES results vs. ICP-MS results. We can see that a reasonably good correlation is found, although concentrations determined via ICP-MS are much smaller. In fig. 3.5, we also introduce IC results for further intercomparison. For clarity, we want to point out that data shown in fig. 3.5 is corrected for the field blanks. Still the differences of the two data sets (with and without correction with field blanks) are quite small, as can be seen from the results of correlation analysis. Taking into consideration that the results of the ICP-OES seem to resemble the actual Ca concentration much better than the ICP-MS measurements, a correction factor was applied to the latter. The average of the difference of the corrected ICP-MS results vs. the ICP-OES results lies in the factor 5,71, consequently, all ICP-MS results were multiplied by that. Compared with the IC results, the ICP-OES results are higher (naturally as IC only detects ions soluble in MSA), but show a clear correlation still, see also fig. 3.5.

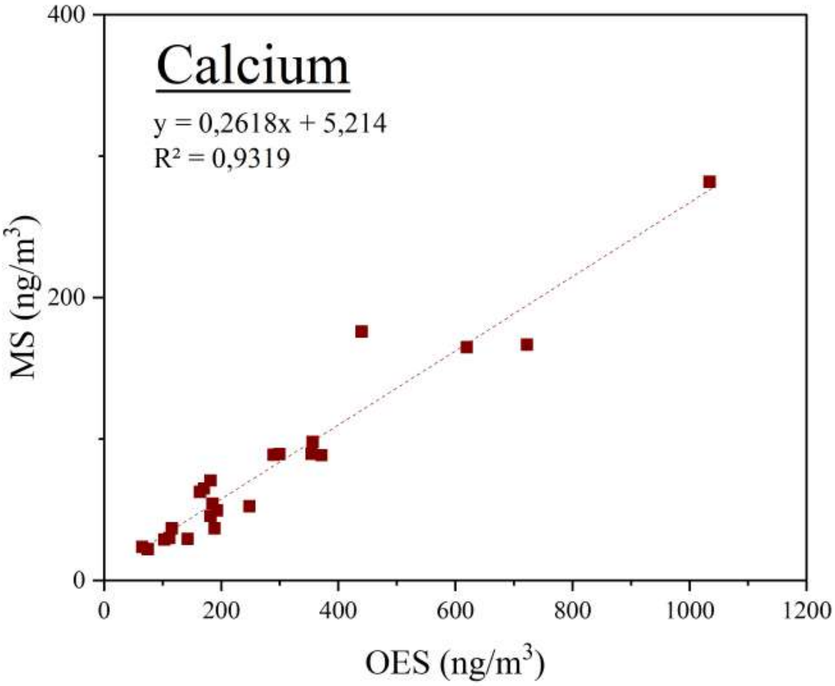

Figure 3.4: Comparison of Ca concentration data for filter measurements obtained by ICP-MS vs. ICP-OES analysis

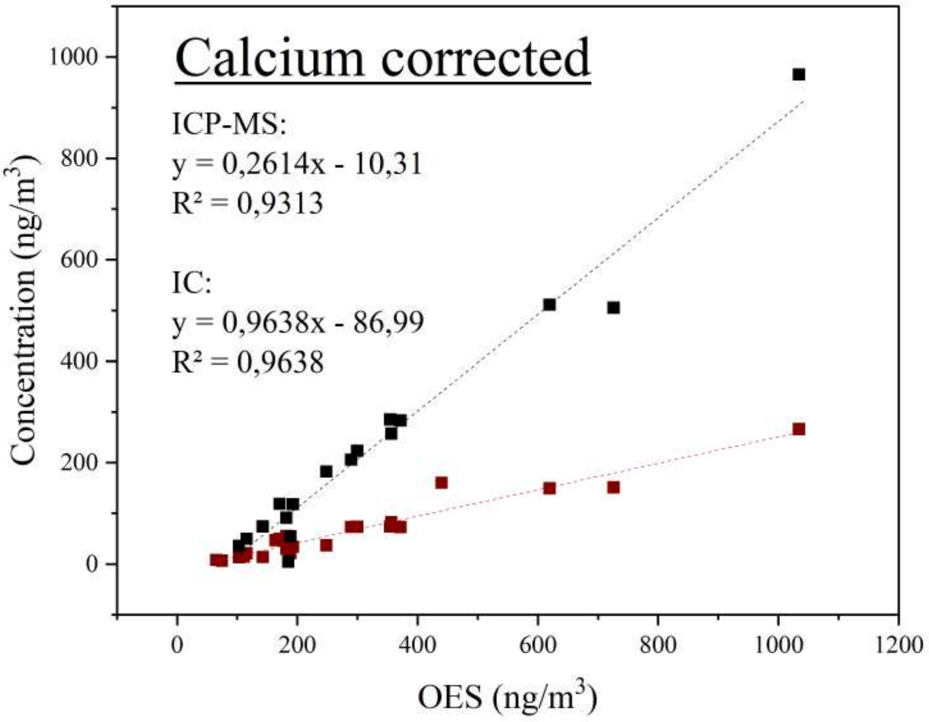

Figure 3.5: Comparison of Ca concentration data for filter measurements, blank corrected, ICP-OES vs. ICP-MS comparison in red, ICP-OES vs. IC comparison in black

3.2 Annual cycles of particulate matter and chemical constituents

3.2.1 Annual cycles of elements

Of the 153 weeks that were considered during this work, only 141 filters could actually be digested due to before mentioned reasons (section 3.1). Besides that, 33 blank filters were digested and evaluated. After the values of the blank filters were converted to atmospheric concentrations using the average air sample volume, the average blank was subtracted. The LOD was defined as the standard deviation of the blank filter measurements. The LOD values for each element can be seen in table 3.2. They were checked against filter results, which were then categorized as above or below the LOD. Results below the LOD were defined as half of the LOD. The number of measurements above and below LOD can also be found in table 3.2.

This gives a first impression of the feasibility of reliable quantification in this context for each element. Mg for example shows a high number of values below the LOD, which is partly due to its low concentration on a lot of filters, but also affected by the relatively high LOD stemming from a high standard deviation. The LOD of Al does not differ much from the one for Mg, but

Table 3.2: LOD values of evaluated elements

	24Mg	27Al	44Ca	48Ti	52Cr	55Mn	56Fe	59Co	61Ni	88Sr	208Pb
Blank filter value (ng/m^3)	47	65	16	1,5	1,4	0,95	16	0,015	1,7	0,69	0,10
Standard deviation (ng/m^3) = LOD	29	15	9,3	1,7	0,33	0,62	3,5	0,011	0,33	0,34	0,086
No. of values above LOD	20	121	81	79	42	45	114	85	45	39	121
No. of values below LOD	121	20	60	62	99	96	27	56	96	102	20

more Al is present on the filters, making the number of invalid values the lowest in this data set. For Al, however, five field blank measurements were omitted, because of especially high values. One may conclude that the method used in this thesis is not suitable for quantification at low concentrations, and might argue for the need of a lower LOD as well; to this it should be said, that the highly loaded filters (i.e. the ones sampled during phases of long range transport mineral dust over Austria) of interest generally show a better relation to the LOD. As explained later (see section 3.3.2), 56 filters showed an influence of mineral dust originating from desert regions. The number of valid measurements exceeds this number for most of the elements. To investigate temporal trends of the elements, however, a lower LOD would be beneficial. Still, the results presented here give a first insight into the conditions at the sampling site. For further calculations, values below the LOD were substituted by the LOD value divided by two.

To start with, yearly trends of the elements were evaluated. This is illustrated in fig. 3.6 and 3.7, based on single samples and monthly averages, including season indicators for the single samples. The different scales in the y-axis should be noted. Seasons were defined by meteorological standards: winter consists of December, January and February, spring consists of March, April and May, summer consists of June, July and August, and fall is defined as September, October and November.

Patterns can be found to be similar for elements that Scheuvens et al. (2013) describe as major elemental contributors to Northern African mineral dusts, such as Al, Fe, Ca, and Mg [16]. Also Ti, Mn and, to a lesser extent, Sr follow this trend. Closer inspection for the correlation with Saharan dust occurrences in the area can be found in section 3.4.

Conditions for Mg are somewhat special (see fig. 3.6a). Looking at the weekly samples, barely any trends throughout the seasons are recognizable. As previously mentioned, a lot of samples have intensities below the LOD, leaving hardly any room for interpretation. A few spikes of concentrations are observed in the summers of 2019 and 2021, and a few additional ones distributed over the other seasons and years, but these do not indicate any reliable regularities. All of them can later be related to long range transport of mineral dust.

The annual cycle for Al (fig. 3.6b) presents more information. We can see obvious spikes in the summers of 2019 and 2021, and more constant activity in the fall and spring time. In the winters as well, a few samples with high concentrations are recorded. The elements Ca (fig. 3.6c), Ti (fig. 3.6d), Cr (fig. 3.6e), Mn (fig. 3.6f), Fe (fig. 3.6g) and Sr (fig. 3.6j) show spike patterns similar to Al. This might be a sign for a common correlation in SDE, which is consistent with literature and will be explored further in the following chapters.

Co (fig. 3.6h) shows a different temporal trend with more spikes visible in the summer of 2020. This might be explainable by construction work done at the observatory in that time frame. Here, also numerous measurements fall below the LOD.

Ni (fig. 3.6i), unlike the other recorded elements, exhibits a number of spikes in the fall of 2021.

For Pb (fig. 3.6k), despite its relatively low concentrations, a comparably high number of results above the LOD was determined. Maximum concentrations tend to be determined in summer, to a lesser extent also in spring and fall.

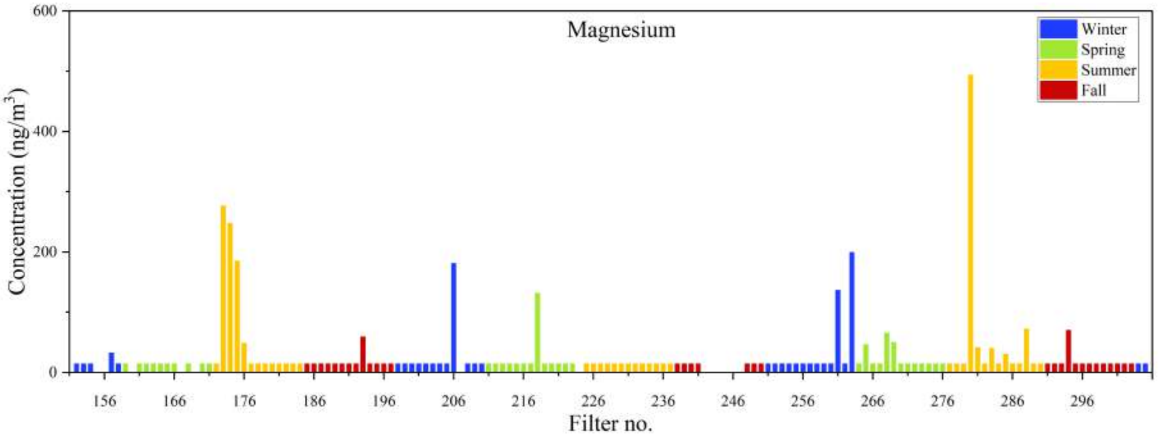

(a) Yearly cycle of Mg

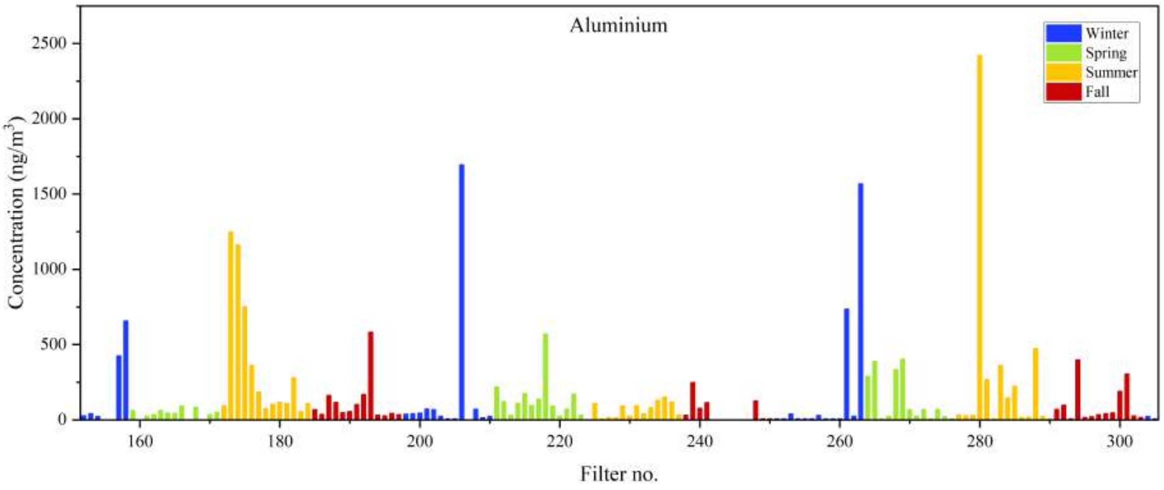

(b) Yearly cycle of Al

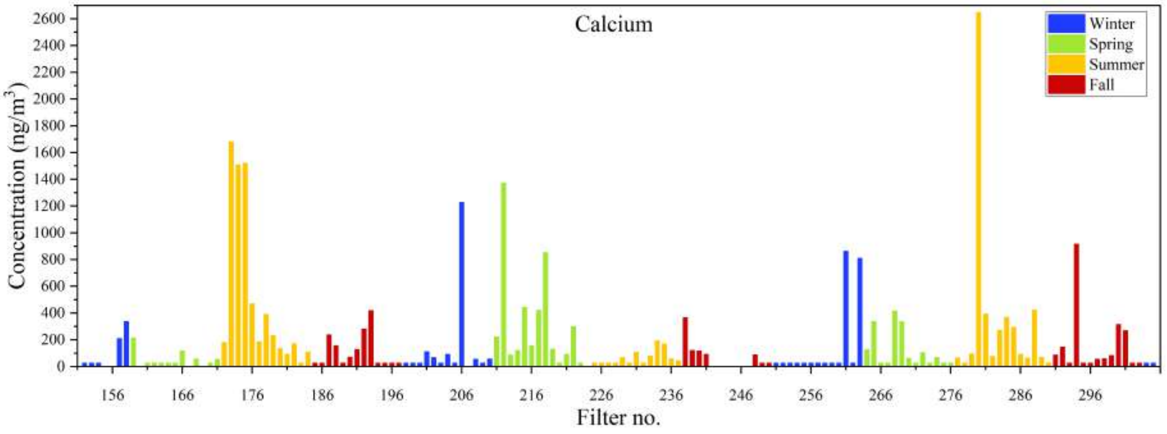

(c) Yearly cycle of Ca

Figure 3.6: Time series of elemental concentrations based on weekly samples

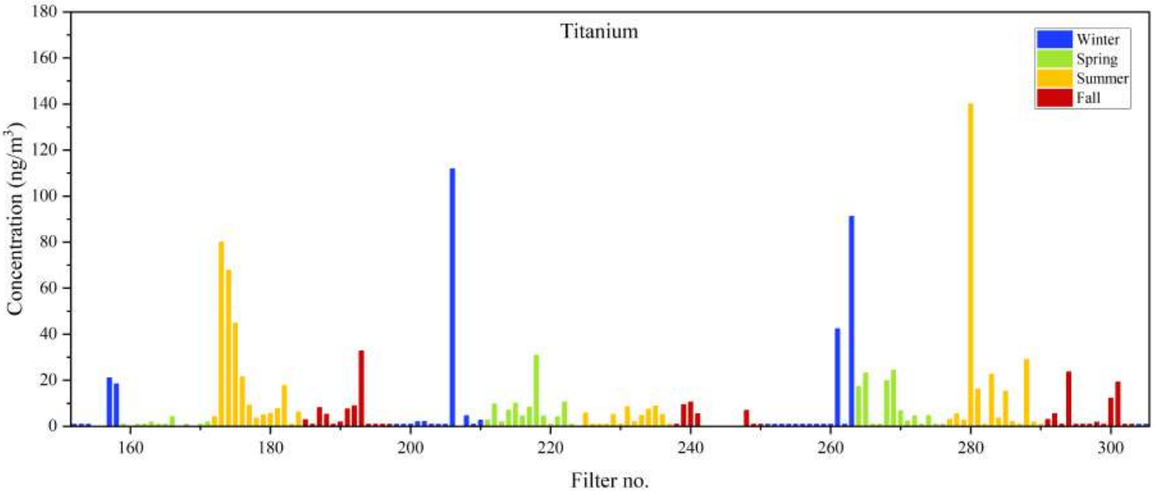

(d) Yearly cycle of Ti

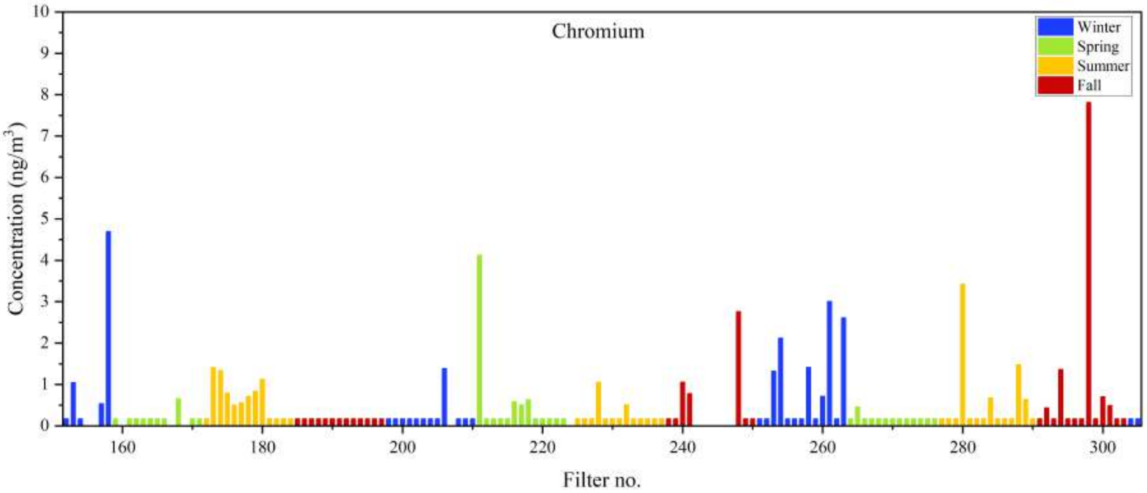

(e) Yearly cycle of Cr

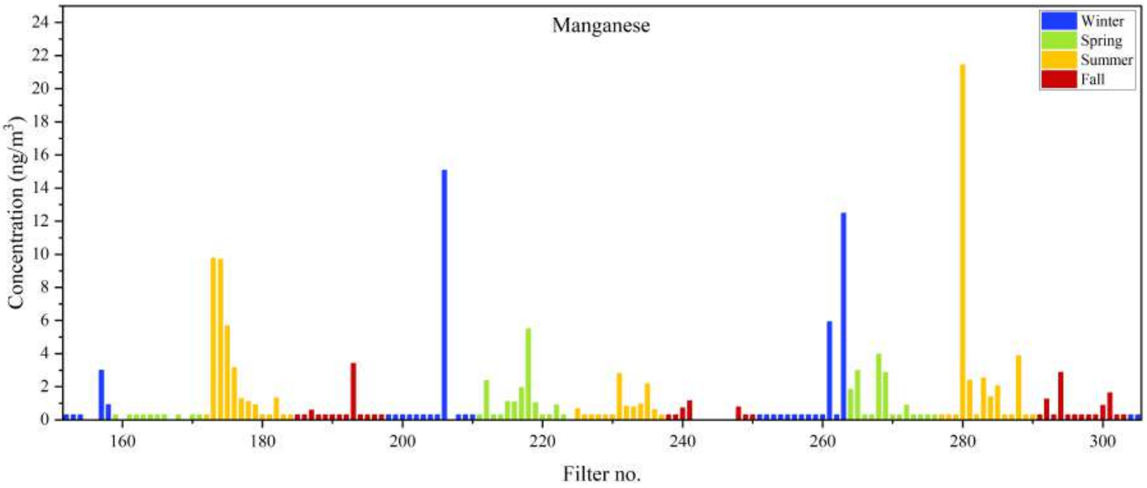

(f) Yearly cycle of Mn

Figure 3.6: Time series of elemental concentrations based on weekly samples

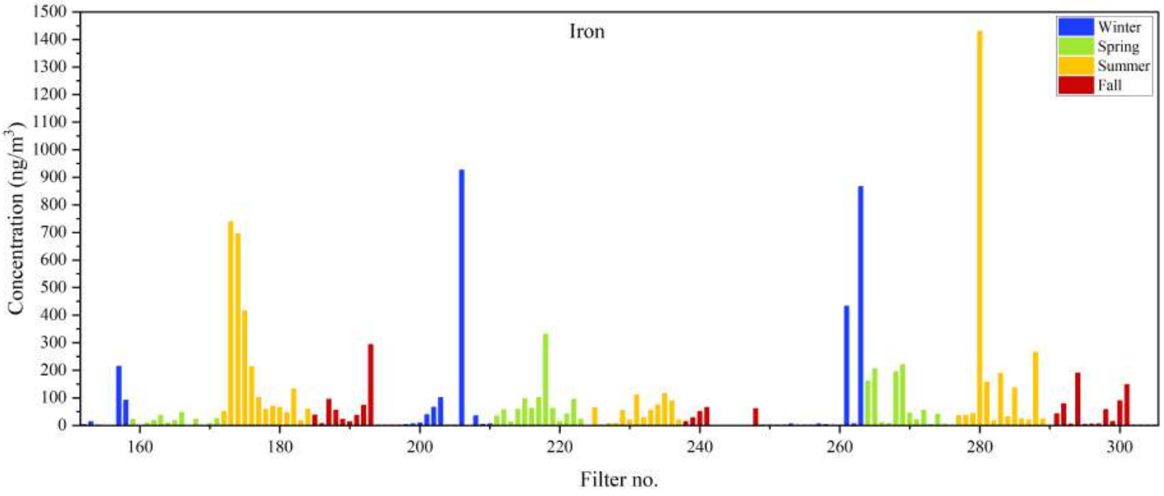

(g) Yearly cycle of Fe

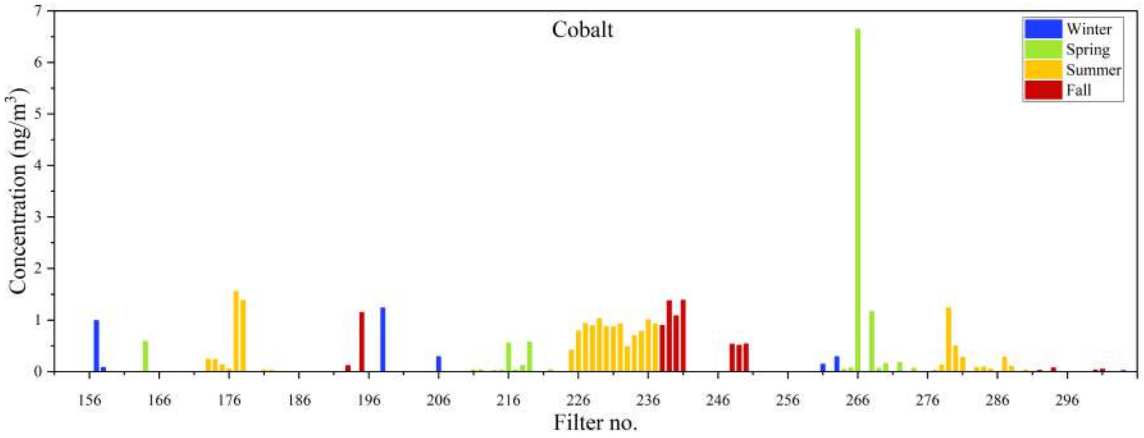

(h) Yearly cycle of Co

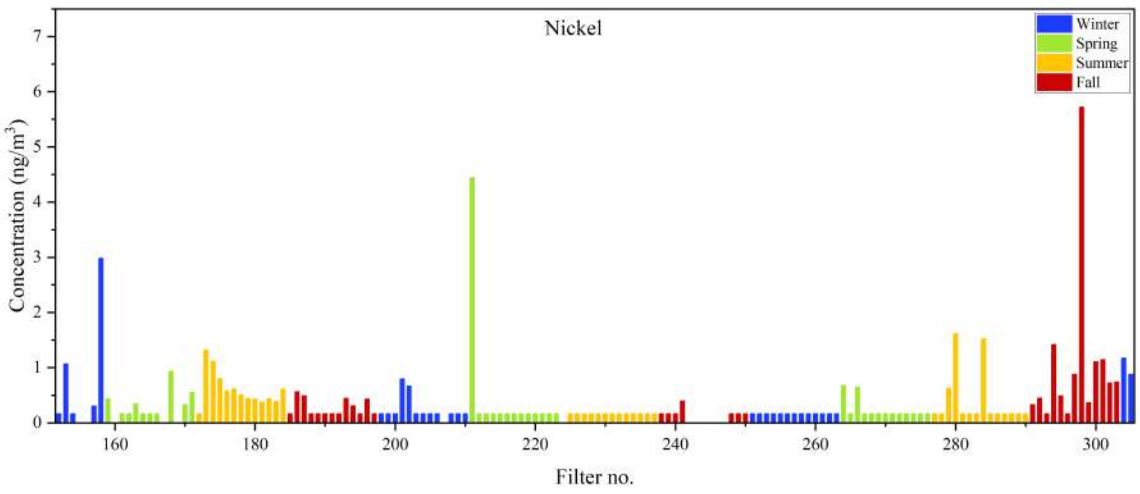

(i) Yearly cycle of Ni

Figure 3.6: Time series of elemental concentrations based on weekly samples

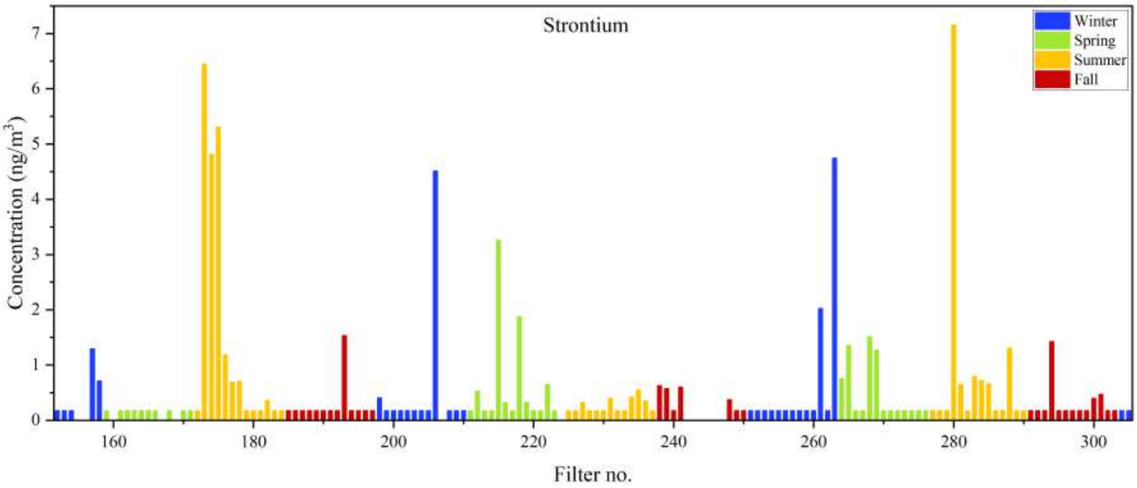

(j) Yearly cycle of Sr

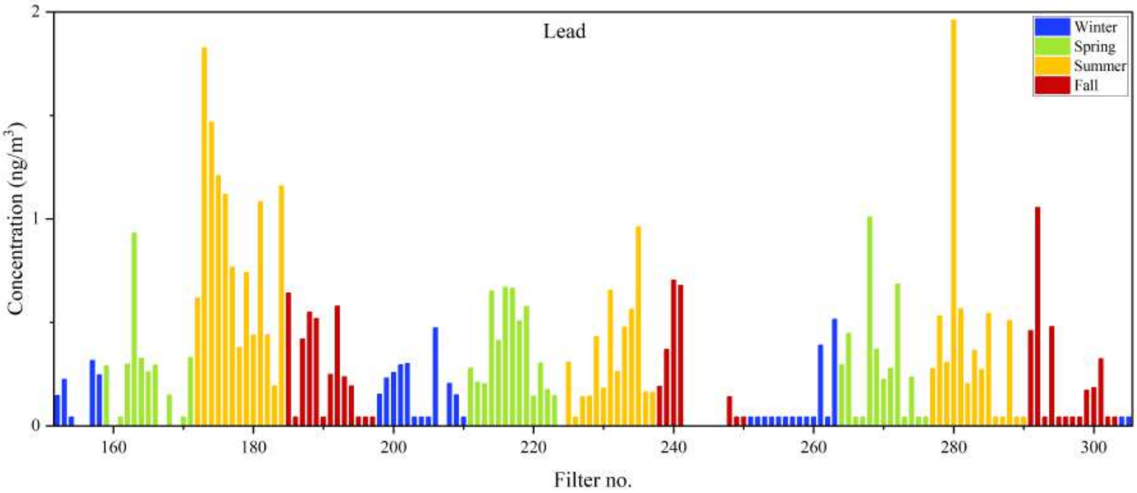

(k) Yearly cycle of Pb

Figure 3.6: Time series of elemental concentrations based on weekly samples

The categorization by month was performed on the basis that a week was counted as belonging to a certain month, if four or more days of that week were in the respective month. Illustration for this can be seen in fig. 3.7. Overall, one can conclude that there is no clear trend that persists in all three years when it comes to monthly averages. Again, elements usually associated with mineral dust (Mg, Ca, Al, Ti, Mn, Fe and Sr) show similar patterns. Elevated monthly averages were determined in several months, but not the same months every year. Elevated concentrations can be detected for most elements in June 2019 and 2021, but not 2020. Higher concentrations can also be seen in March 2021 and to a lesser extent also in March 2019. Constantly low results for almost all elements and months are seen in November and December. Elemental concentrations seem to be affected strongly by Sahara dust occurrences, which will be explored within this thesis in later sections (see e.g. section 3.3). From various literature data considered, expected elevated concentrations would be found in the spring and summer time [5]. Some elements stray from these mineral dust affiliated elements, namely Ni, Co, Cr and Pb. Pb is special, as it seems to follow a trend similar to expected yearly cycles influenced by anthropogenic sources from boundary layer air, i.e. concentrations are higher in summer than in winter.

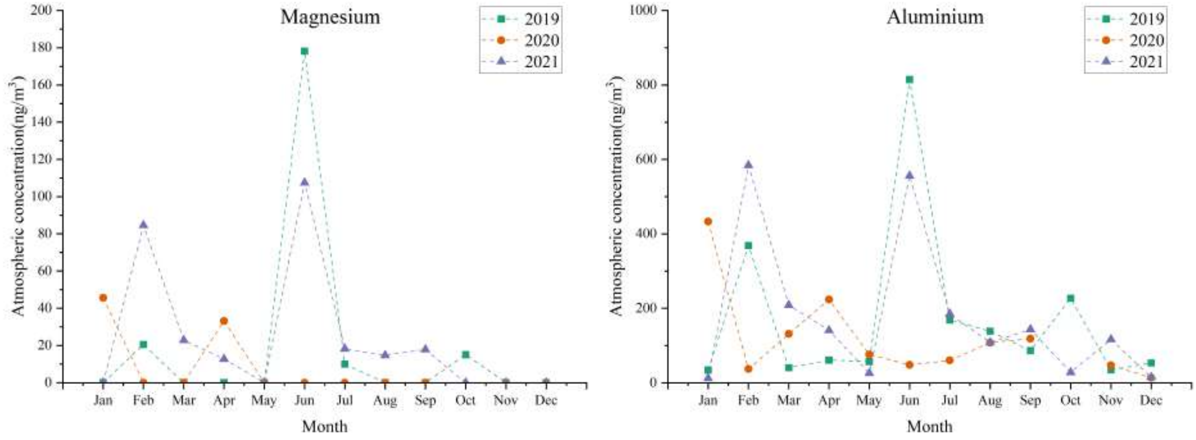

(a) Yearly cycle of magnesium

(b) Yearly cycle of aluminium

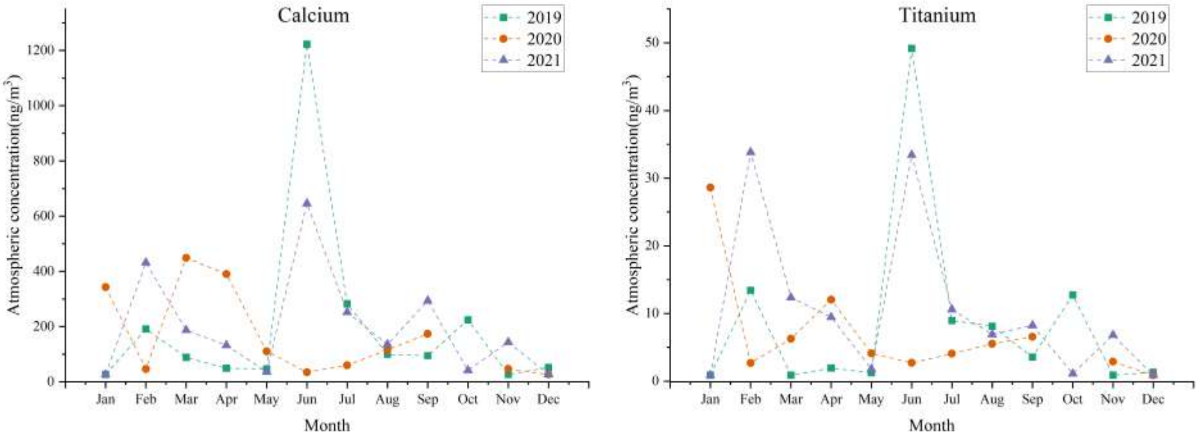

(c) Yearly cycle of calcium

(d) Yearly cycle of titanium

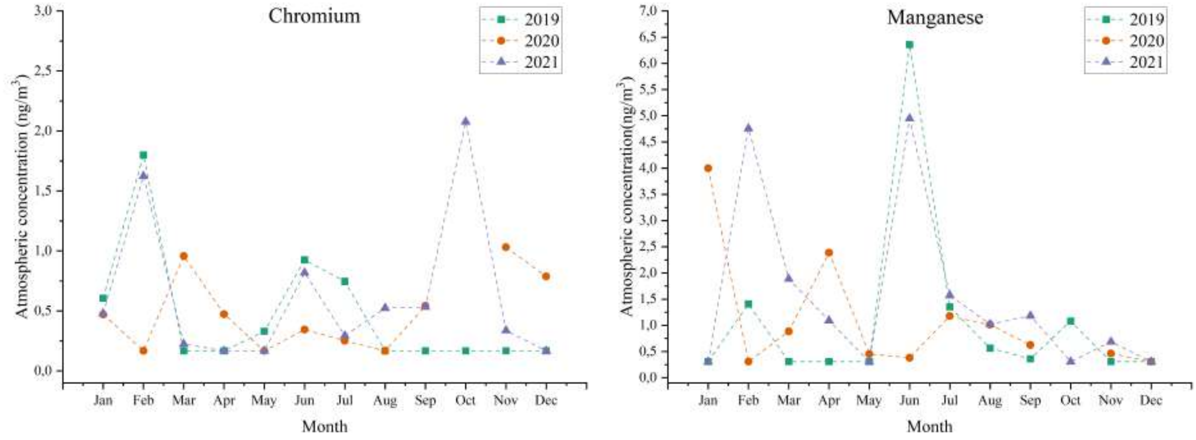

(e) Yearly cycle of chromium

(f) Yearly cycle of manganese

Figure 3.7: Time series of elemental concentrations based on monthly averages

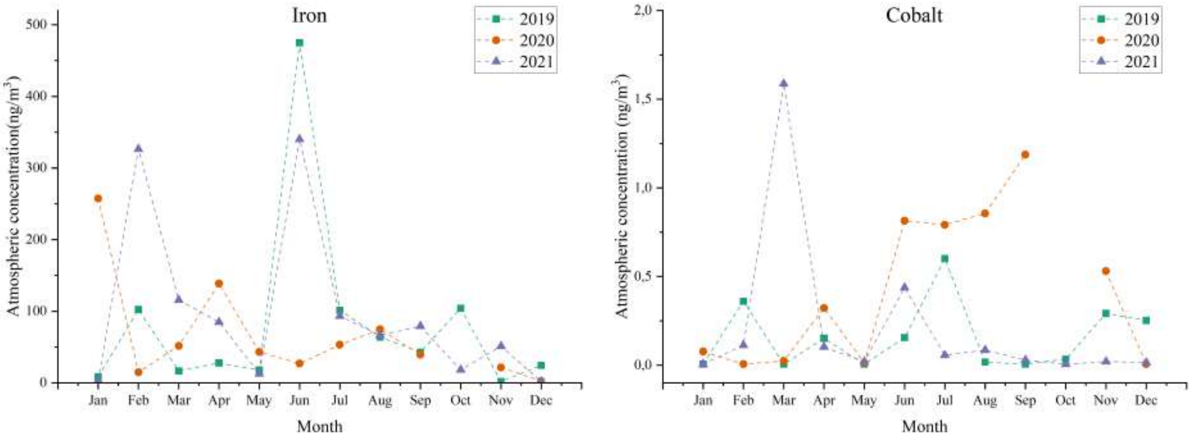

(g) Yearly cycle of iron

(h) Yearly cycle of cobalt

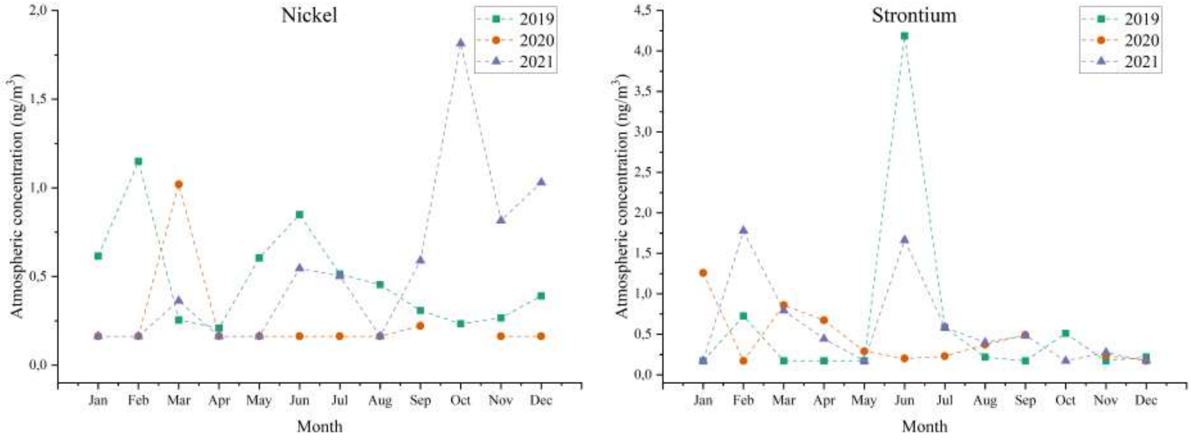

(i) Yearly cycle of nickel

(j) Yearly cycle of strontium

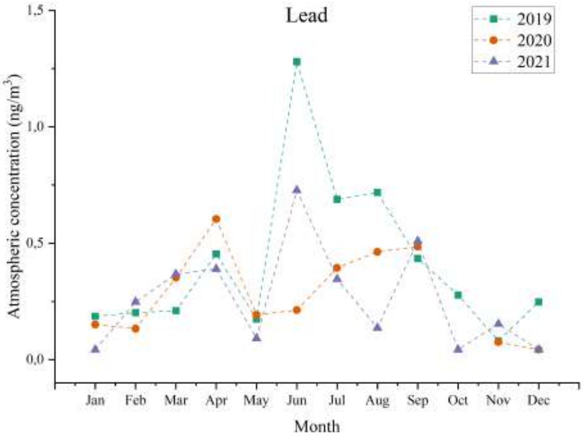

(k) Yearly cycle of lead

Figure 3.7: Time series of elemental concentrations based on monthly averages

3.2.2 Annual cycles of MSA-soluble ions

Looking at concentration values determined by ion chromatography (i.e. compounds soluble in 30 mM MSA), and their temporal patterns, additional conclusions can be drawn. For soluble magnesium (fig. 3.8a), the LOD achieved by IC is low enough to show an annual trend. We can see, however, that the highest concentrations are detected in a similar manner as they were in fig. 3.6a. For calcium and its IC measurement (fig. 3.8b), we can see similar pattern as in fig. 3.6c between the two, with the high peaks being the same filters. Overall, we can see that again, the summers of 2019 and 2021 show higher concentrations for these elements, while the summer of 2020 deviates from this. When looking at potassium (fig. 3.8c), we see elevated concentrations most often in spring, summer and fall, and only a few of them in the winter time. Potassium ions seem to not be strongly linked to SDE, other possible sources could be e.g. wood combustion [38]. For sulphate (SO_4^{2-}, 3.8d), we observe also higher concentration in the spring, summer and fall, and in the winter time only low concentrations, with no visible exceptions. The results for sulphate are presented as an example for a secondary aerosol compound and the influence boundary layer air masses have on the conditions at the site.

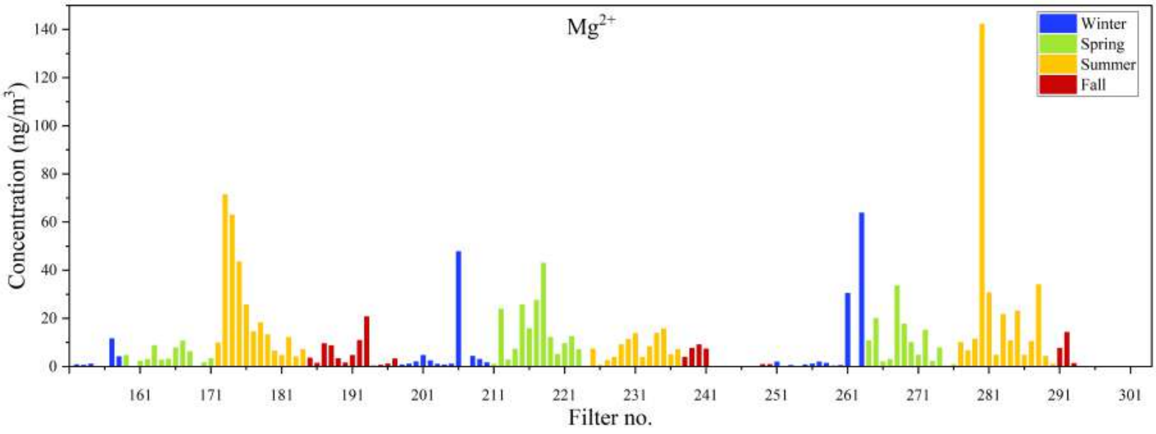

(a) Yearly cycle of Mg^{2+}

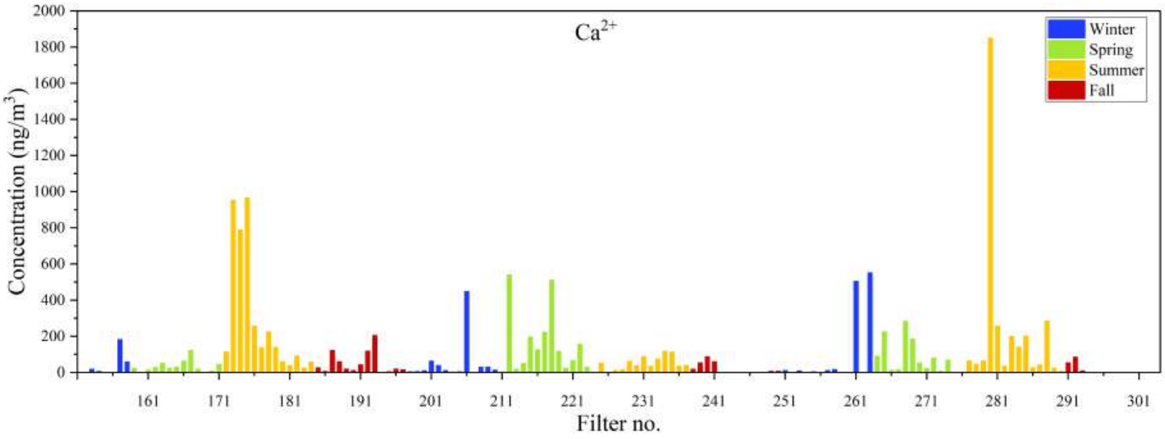

(b) Yearly cycle of Ca^{2+}

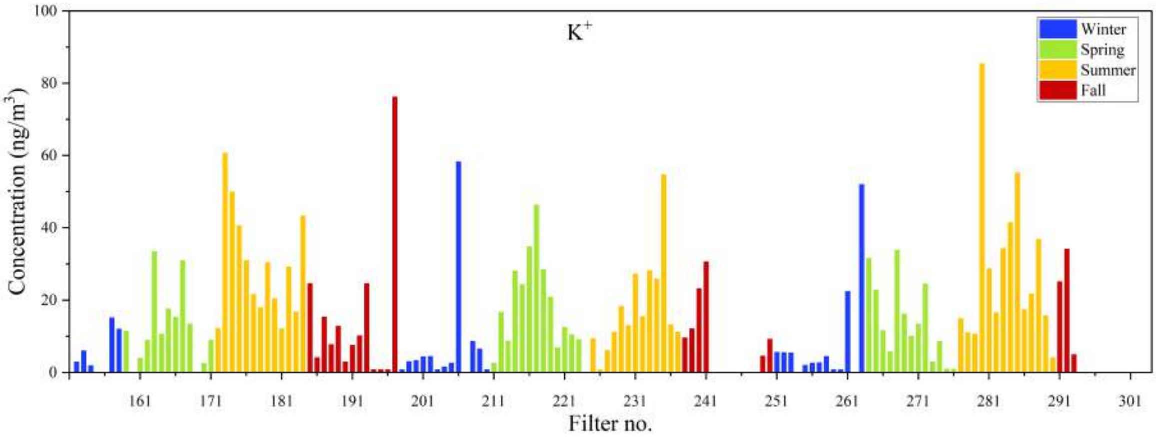

(c) Yearly cycle of K^{+}

Figure 3.8: Time series of concentration data based on weekly samples, obtained by IC

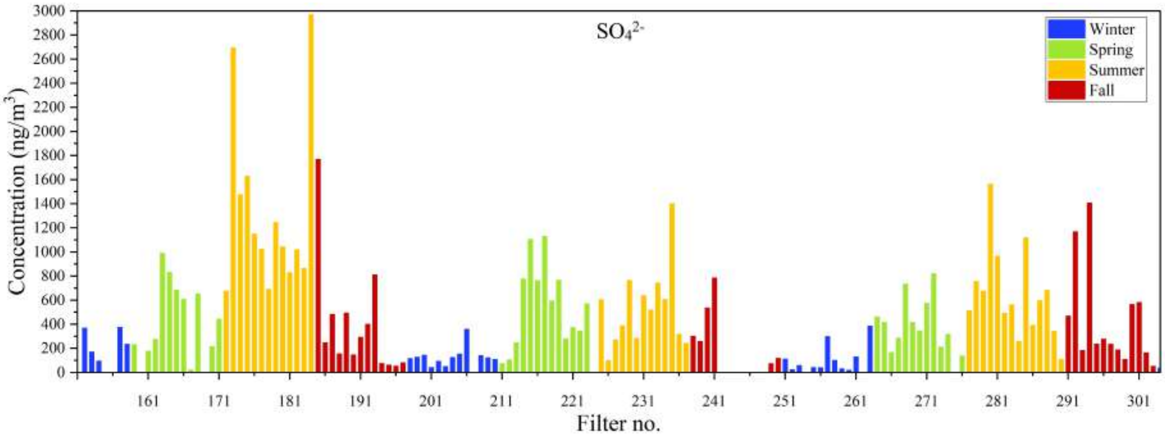

(d) Yearly cycle of SO_4^{2-}

Figure 3.8: Time series of concentration data based on weekly samples, obtained by IC

3.2.3 Yearly trend of TSP mass

In order to compare the amount of dust we are able to analyze using this method with the overall PM mass, data of TSP mass collected by a Sharp monitor was used. For better comparability, the 30-min averages taken from the β-attenuation monitoring were averaged to align them with the weekly filter data. In fig. 3.9, we can see the TSP over the three years examined in this thesis. Again, we see higher concentrations in the summers of 2019 and 2021, with summer 2020 deviating. In fig. 3.10 TSP is also shown as monthly averages. Overall, elevated concentrations can be detected in spring, summer and fall, with only a few exceptionally high values in winter time. Highest concentrations of TSP are in agreement with highest concentrations of the single elements, especially mineral dust markers like Al and Fe.

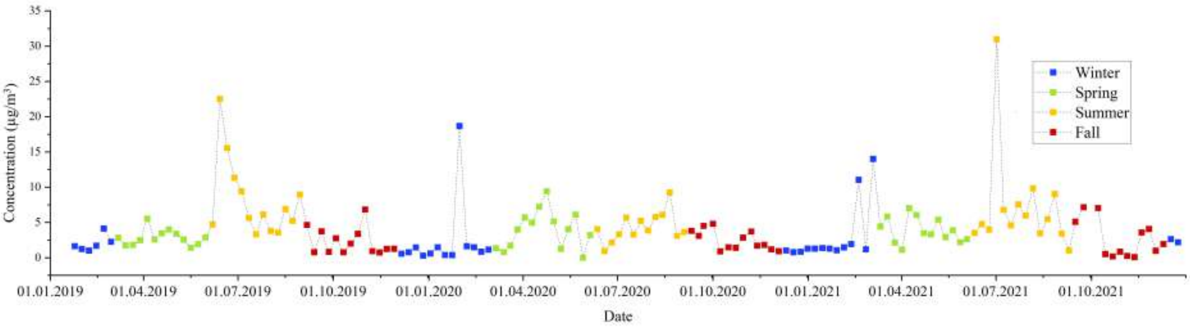

Figure 3.9: Time series of TSP concentration data 2019-2021 based on weekly samples

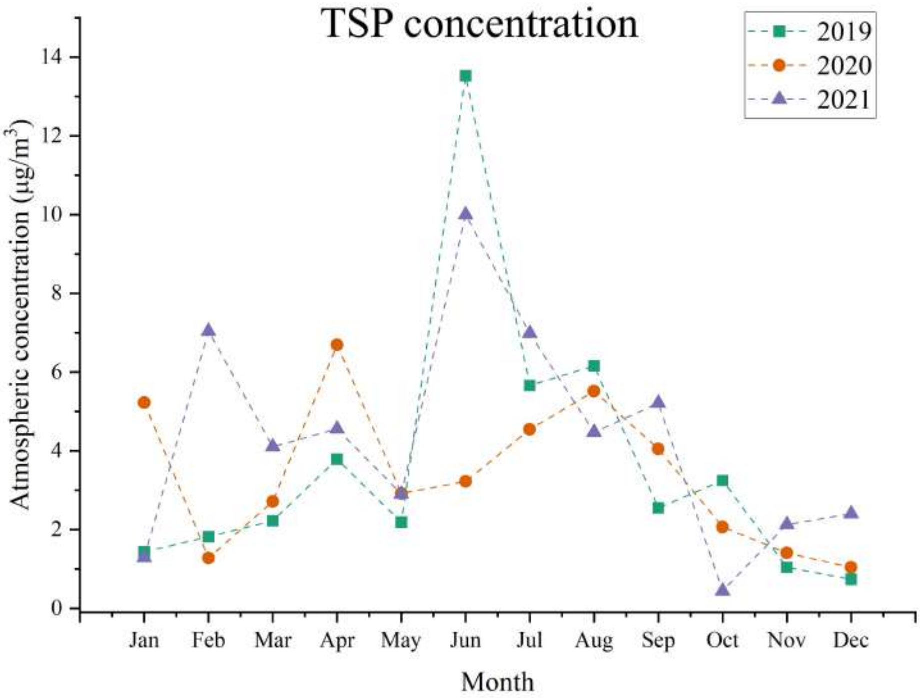

Figure 3.10: Annual cycles of TSP concentration data based on monthly averages

3.3 Identification of Sahara dust events via modelling

To obtain insight into the occurrences of Sahara dust events in the Eastern alpine region, modelled data was used. The data is provided by ZAMG and uses a WRF-Chem model based on Grell et al. 2005 [39]. In these calculations, a relationship between air chemistry and meteorology is established considering factors such as radiation, precipitation, temperature, to include direct, indirect and semi-direct forms of effects. The complete parameters of the data modelling can be read in Baumann-Stanzer et al. 2019 [27]. The data is presented as images, for which two examples are provided in fig. 3.11.

The images were visually investigated for their prediction of occurrence of Sahara dust over Austria and put into binary categories for each picture, positive or negative for an occurring Sahara dust event. Days with missing model calculations are also indicated, and the count of the categorized days can be seen in table 3.3. Pey et al. 2012 [40] found that less than 20% of days annually of European sites north of the Mediterranean basis experience dust outbreaks. Considering our numbers gathered from the modelled data, similar results are found. The average amount of days per year categorized positively for SDE in the three years considered is 13%, with the percentage of data missing at 7%. Greilinger et al. 2018 [15] speak of up to

30 days per year of mineral dust influence on the observatory itself which is considerably lower than findings here. However, this could be an effect of our evaluation from the modelled images for the region of entire Austria, not just directly above the location of the SBO.

Table 3.3: Statistics on the occurrence of SDE in Austria, n = number of days, % = days as percentages based on 365 days per year

	2019		2020		2021		
	n	%	n	%	n	%	Average %
SDE positive	56	15%	34	9%	47	13%	13%
SDE negative	285	78%	311	85%	285	78%	79%
No data available	24	7%	21	6%	33	9%	7%

Examples of a picture resulting in a negative rating can be seen in fig. 3.11a, an example for a positive rating is depicted in fig. 3.11b. Images are provided in a resolution of 12 hours.

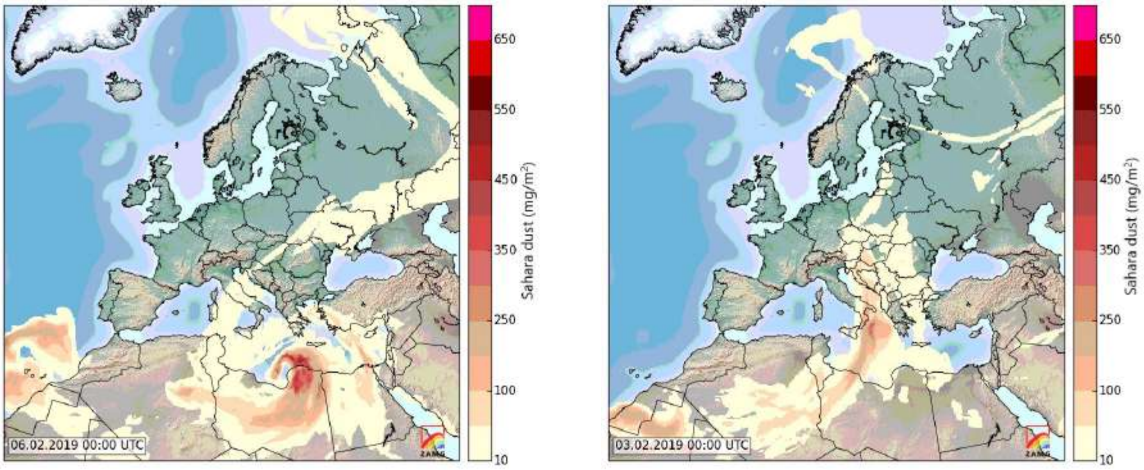

(a) Model image rated negative for SDE (b) Model image rated positive for SDE

Figure 3.11: Modelled images regarding SDE obtained from ZAMG

Because of the temporal resolution of the filter data given to be a week, the modelled images were also combined into weekly categories. By doing so, only weeks with available filters are accounted for, the rest were left out. Category 0 describes weeks in which the week itself is not affected by Saharan dust occurrences, nor the week before or afterwards. Category 1 and 2 describe weeks that are themselves not affected by Sahara dust occurrences, but the week before or after (either days further away or closer to the week actually considered) are. These two categories are implemented separately to investigate potential dust loads that may already be in the atmosphere before, or that still linger after a Sahara dust occurrence. Category 3 describes a week that is affected by Sahara dust occurrences for up to two days out of the week, weeks in category 4 are influenced by Sahara dust occurrences for 3 days or more. The results of this classification are summarized in table 3.4.

Table 3.4: Evaluation of SDE occurrence into 5 different categories according to frequency

		No. of weeks			
Category	Classification	2019	2020	2021	Total
Week without SDE in week, before or after	0	18	16	13	47
Week without SDE (but SDE 3+ days before/after)	1	10	11	11	32
Week without SDE (but SDE up to 2 days before/after)	2	3	5	6	14
Week with SDE (up to 2 days)	3	9	9	12	30
Week with SDE (3+ days)	4	10	6	10	26

3.4 Elemental composition of PM with and without the influence of Sahara dust events

To gain insight into how the average dust influx at SBO is composed, the average concentrations of the elements analyzed are compared to the overall aerosol mass, to be seen in fig. 3.12. For this, the elemental data obtained via ICP-MS was compared with the TSP mass concentration supplied by the β-attenuation monitor.

3.4.1 Determination of the silicon content

Since silicon could not be measured directly because of the quartz filter material, the silicon concentration had to be approximated. In related literature, the mass ratio of Si to Al is often used. For this, different publications report different findings. In Formenti et al. 2014, Si/Al ratios range from 1,5 to about 4, depending on the origin location in West Africa [41]. In Carrico et al. 2003 [42], investigating aerosol properties in Nepal, the ratio of Si/Al is reported as 2,5±0,2. Earlier works describe the Si/Al ratio to be around 2-2,5 [43, 44]. In the Commission Staff Working Paper by the European Commission on the directive 2008/50/EC, a ratio of Al_2O_3 to SiO_2 of 3 is described for the validation of the method of quantification of SDE [5].

To select a ratio for our sampling, additional elemental data of the mineral dust found in the SBO area was obtained with an XRF spectrometer by analyzing snow samples taken in the vicinity of the Digitel measuring station. Three of the described snow samples (see section 2.6) from different days were analyzed, the percentages for the elements Al and Si can be seen in table 3.5. The average result of Al/Si of 2,56 is in relatively good agreement with the literature values mentioned before. Therefore, for further calculations, the Si/Al ratio suggested by Carrico et al. 2003 [42] of 2,5 was used.

Table 3.5: Mass percentages of elements Si and Al and their ratios

	16.03.2022	20.03.2022	27.03.2022	Average
Si	23,81%	23,64%	27,34%	24,93%
Al	10,03%	10,00%	9,25%	9,76%
Si/Al ratio	2,37	2,36	2,96	2,56

3.4.2 Elemental composition of PM

In fig. 3.12, we can see the elemental composition of the PM10 samples shown using the average elemental concentrations obtained by ICP-MS. The most abundant element here is Si, which can be connected to the high amount of SiO_2 in the mineral dust. There are also considerable amounts of Ca and Al to be found, as well as Fe. As minor components Mg, Cr, Co, Ni, Sr, Pb, and Mn can be identified. The majority of TSP mass remains, in this work, unidentified particulate matter. Inorganic ions like sulphate, nitrate and ammonium and carbonaceous particles contribute to this part.

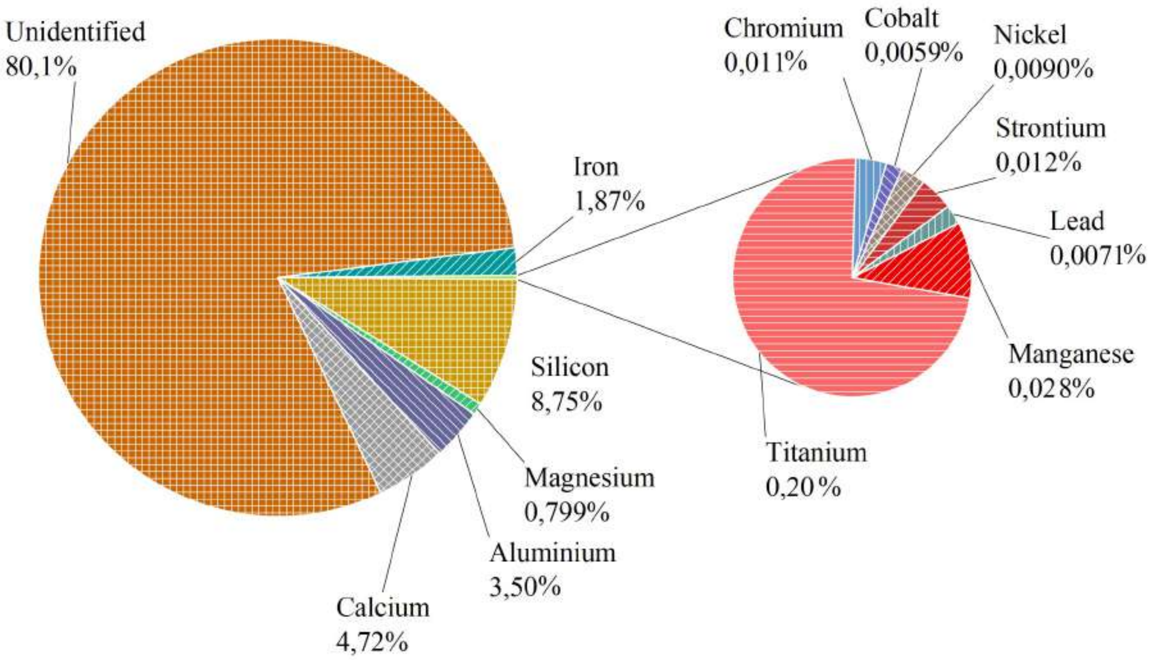

Figure 3.12: Composition using average elemental concentrations from PM10 sampling compared with total suspended particle average

Contrasting this with a specific week of sampling, we see that weeks with a strong Sahara dust influence show different dust composition. In fig. 3.13, we see the composition of the filter with the highest sum of analyzed elements by ICP-MS, filter no. 280 (week 14.06. - 24.06.2021. Compared to the average dust sample shown in fig. 3.12, around 20% more of TSP mass can be explained by elemental analysis. Besides that, patterns of what elements dominate the composition seem fairly similar to the average sample. Silicon shows again the highest contribution, followed by Ca, Al, Fe, Mg, and as minor components Ti, Mn, Sr, Cr, Pb, Ni, and Co.

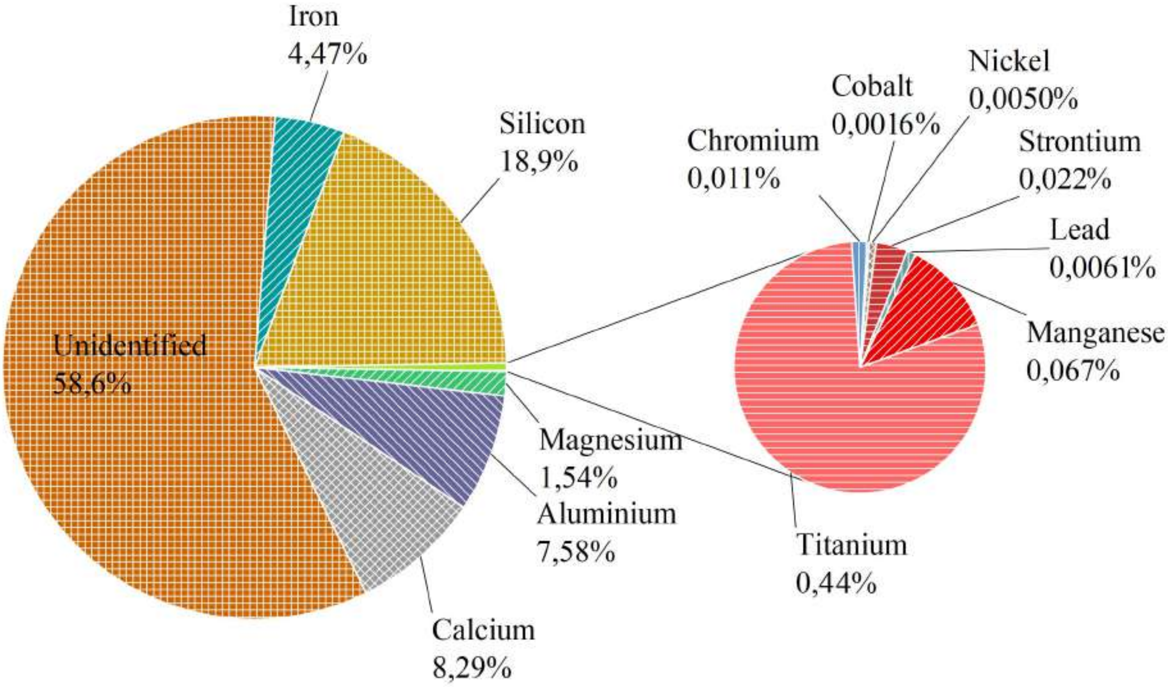

Figure 3.13: Elemental composition of week 14.06. - 24.06.2021 (Filter no. 280)

When we evaluate the average atmospheric concentrations further, combined with the SDE categories, we can also have a closer look into what kind of elements might be more important for the mineral dust events. In table 3.5, we can see the average elemental concentrations of all filters analyzed in their respective assigned SDE categories. The colors used in this table highlight the respective concentration, with dark green being the lowest. Colors then gradually change from green to red, with deep red signifying the highest average concentration of the element in question.

Table 3.6: Average elemental concentrations connected to categories

	Average atmospheric concentration of analyzed element (ng/m^3)									
Categories	Magnesium	Aluminium	Calcium	Titanium	Chromium	Manganese	Iron	Cobalt	Nickel	Strontium	Lead
0	17,3	84,1	145	4,72	0,462	0,698	48,6	0,295	0,380	0,301	0,314
1	16,2	74,3	84,9	3,34	0,469	0,540	28,1	0,453	0,399	0,250	0,258
2	19,6	81,1	127	4,17	0,283	0,809	39,5	0,178	0,357	0,342	0,229
3	27,8	145	201	8,19	0,634	1,17	80,5	0,167	0,533	0,577	0,347
4	77,7	473	470	28,4	0,688	3,76	267	0,185	0,413	1,65	0,494

For most elements analyzed, the highest concentrations can be found in the category which indicates strong occurrences of dust in the described weeks (category 4). In category 4 we see values up to approximately nine times higher than in the category with the lowest average, e.g.

for Fe. The only two exceptions here are Co and Ni, which show no obvious correlation with the SD occurrence. In general, one can see that categories 0, 1 and 2 do not differ much compared to the higher categories. Categories 1 and 2 may even show lower values than category 0. Category 3 and 4 are in line with what is expected for samples affected by desert dust. These findings suggest that the results from analysis of the filters and the modelled data are well aligned.

In the temporal trends of weekly samples in fig. 3.14, similar observations can be made. Here, the bars showing the results of the single samples are colored to represent the earlier mentioned categories of SDE influence. The background shadings represent the different seasons, using the same colors as in fig. 3.6. In contrast to the relatively weak correlation with the seasons, correlation with Sahara dust occurrences is notably stronger. Once again we see that most peaks in higher concentration ranges coincide with dust-heavy weeks. This can be concluded for elements like Mg (fig. 3.14a), Al (fig. 3.14b), Ca (fig. 3.14c), Ti (fig. 3.14d), Mn (fig. 3.14f), Fe (fig. 3.14g), and Sr (fig. 3.14j). No strong correlation between Saharan dust influx and the concentration seems to exist for elements Cr (fig. 3.14e), Co (fig. 3.14h), and Ni (fig. 3.14i). For Pb (fig. 3.14k), the picture is not conclusive; several high concentration values are recorded during dust heavy weeks, but weeks without dust occurrences also show relatively high atmospheric concentrations.

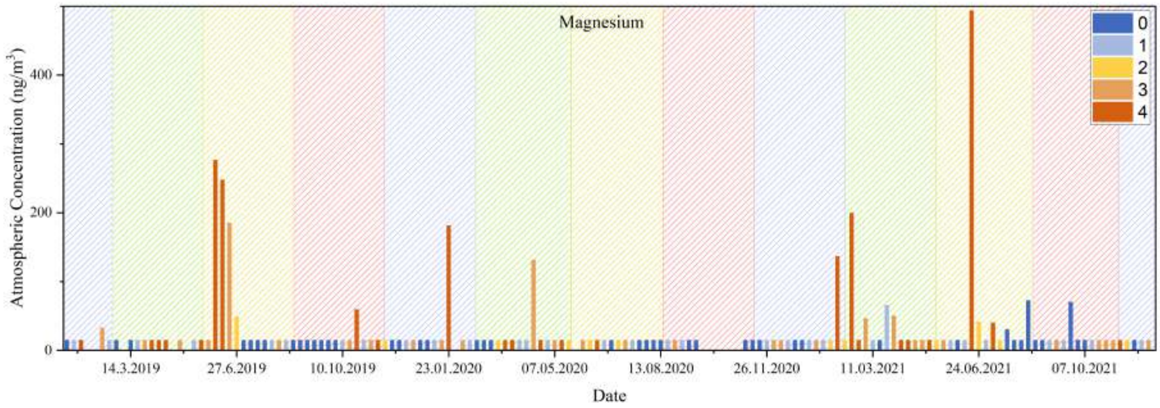

(a) Yearly cycle of Mg, SDEs indicated

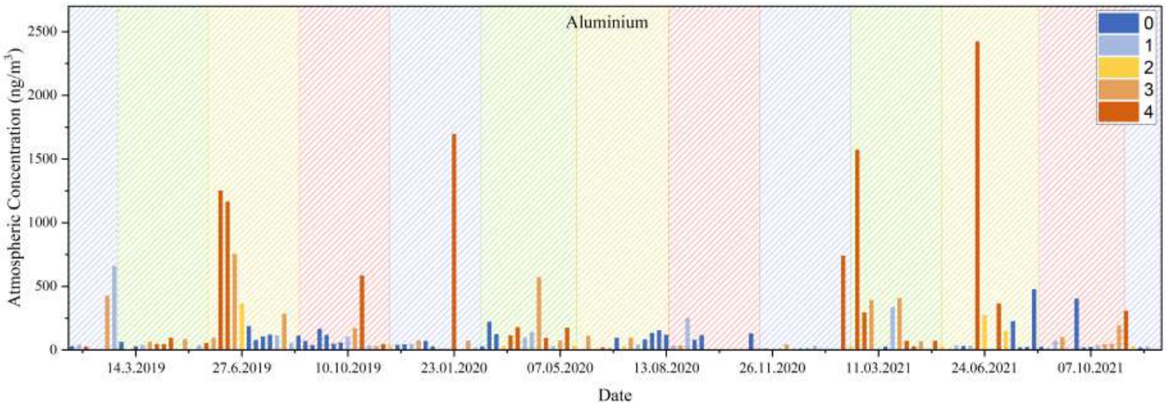

(b) Yearly cycle of Al, SDEs indicated)

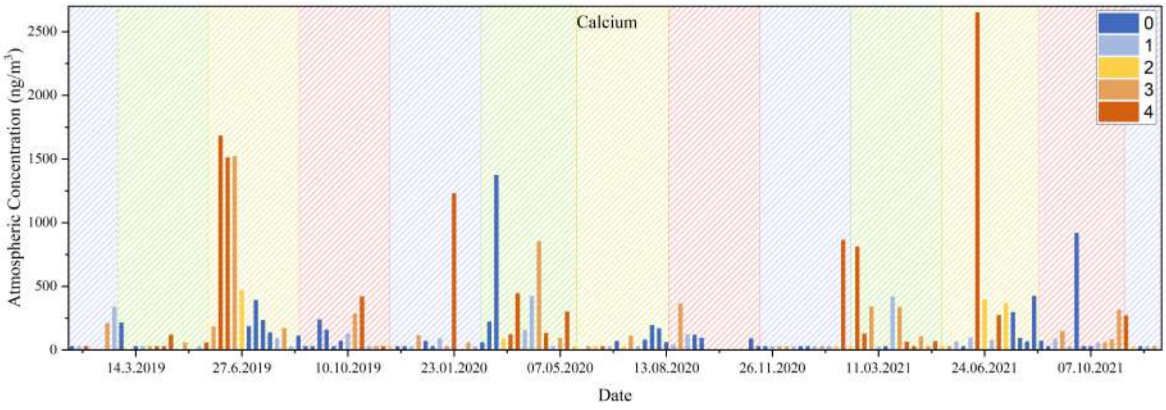

(c) Yearly cycle of Ca, SDEs indicated

Figure 3.14: Time series of elemental concentrations based on weekly samples, with SDE categories indicated, seasons as background (legend for seasons see 3.6)

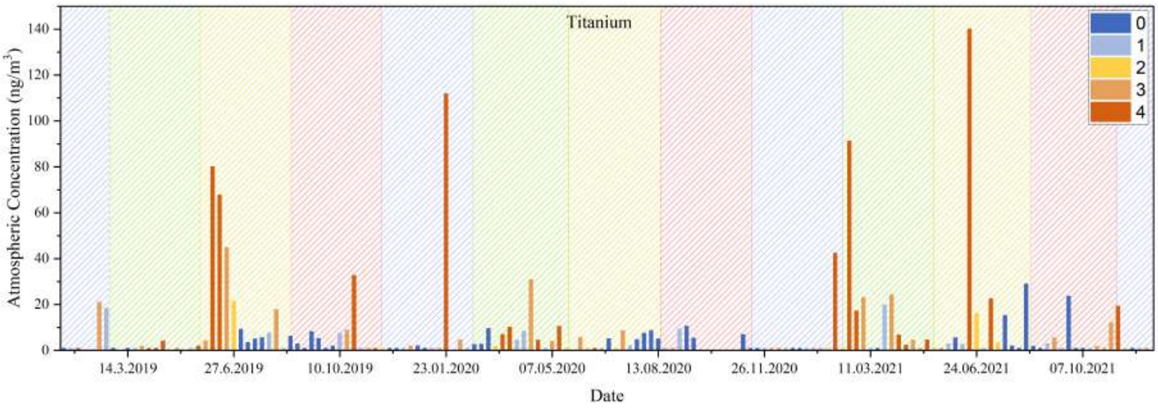

(d) Yearly cycle of Ti, SDEs indicated

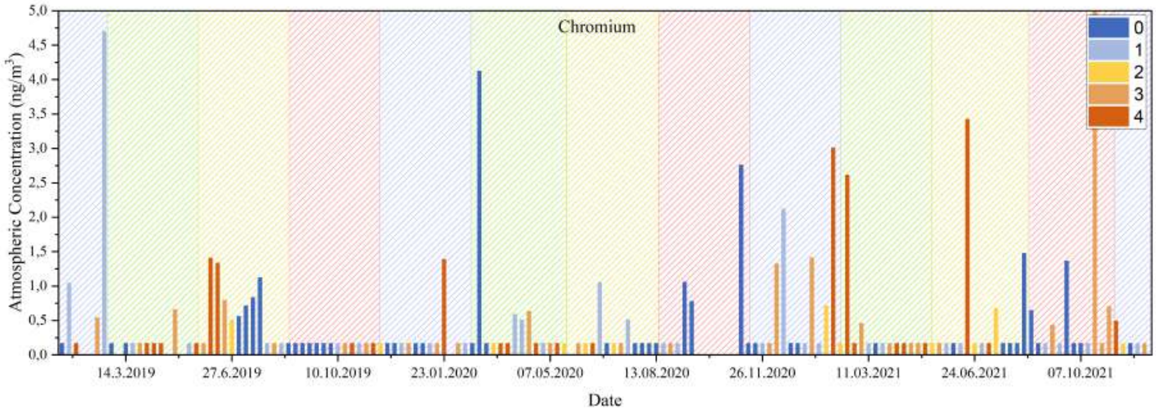

(e) Yearly cycle of Cr, SDEs indicated

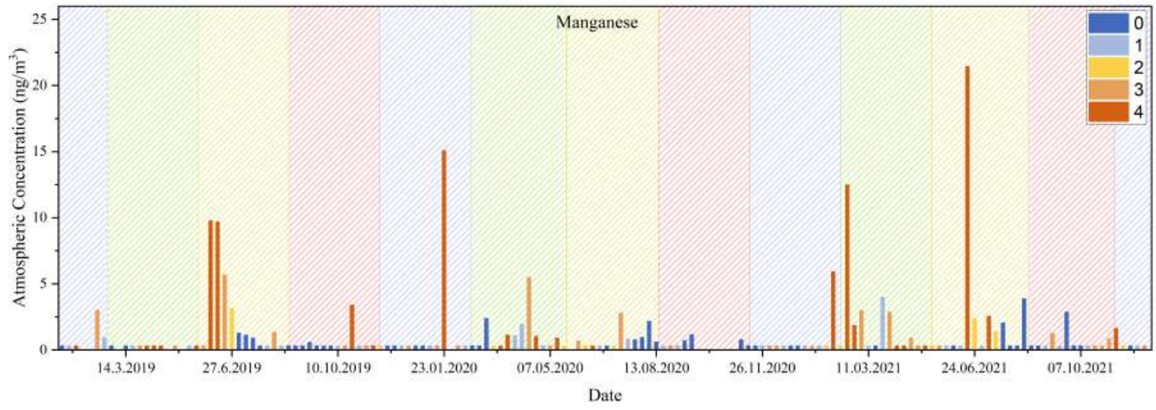

(f) Yearly cycle of Mn, SDEs indicated

Figure 3.14: Time series of elemental concentrations based on weekly samples, with SDE categories indicated, seasons as background (legend for seasons see 3.6)

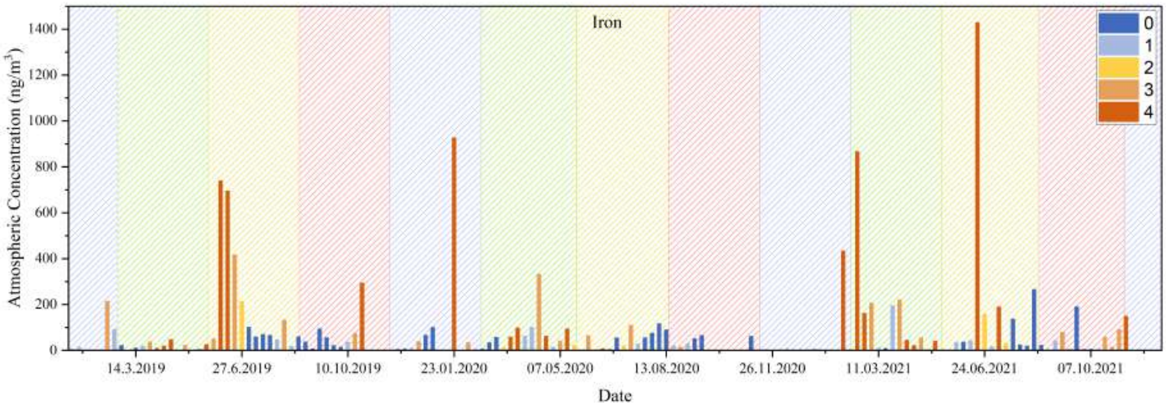

(g) Yearly cycle of Fe, SDEs indicated

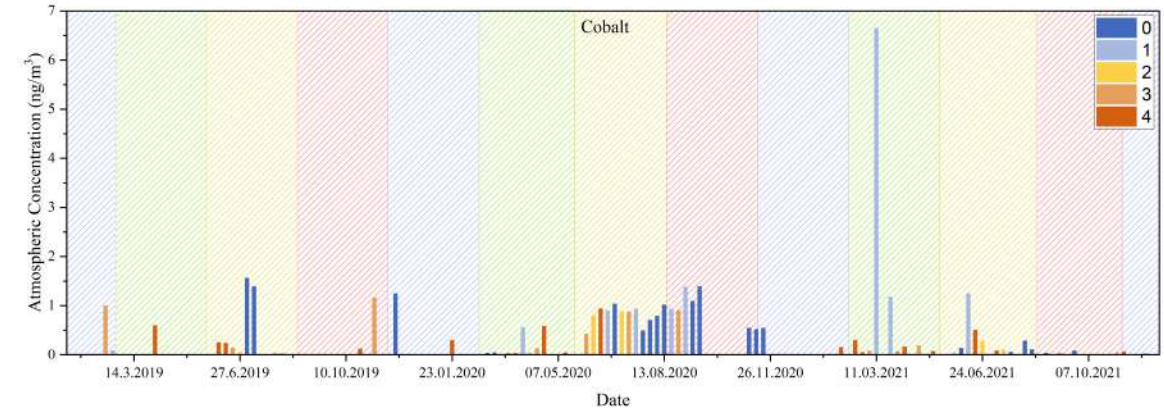

(h) Yearly cycle of Co, SDEs indicated

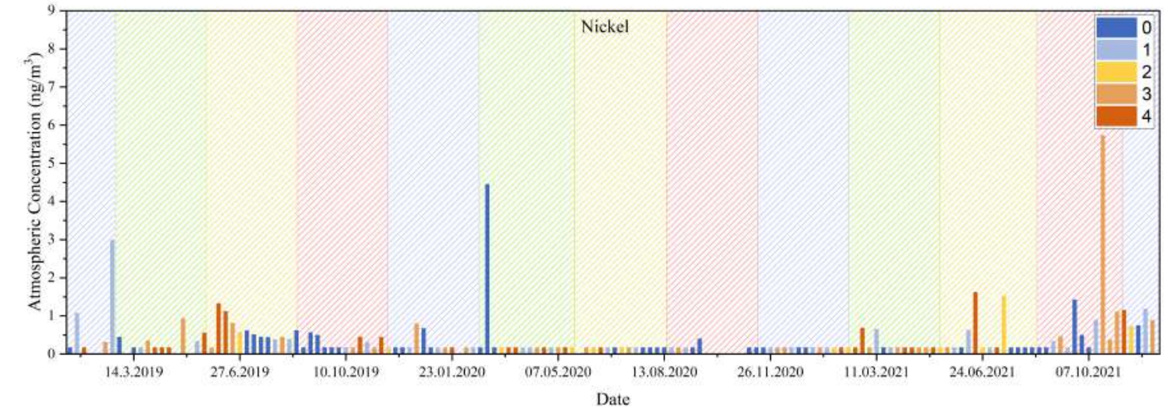

(i) Yearly cycle of Ni, SDEs indicated

Figure 3.14: Time series of elemental concentrations based on weekly samples, with SDE categories indicated, seasons as background (legend for seasons see 3.6)

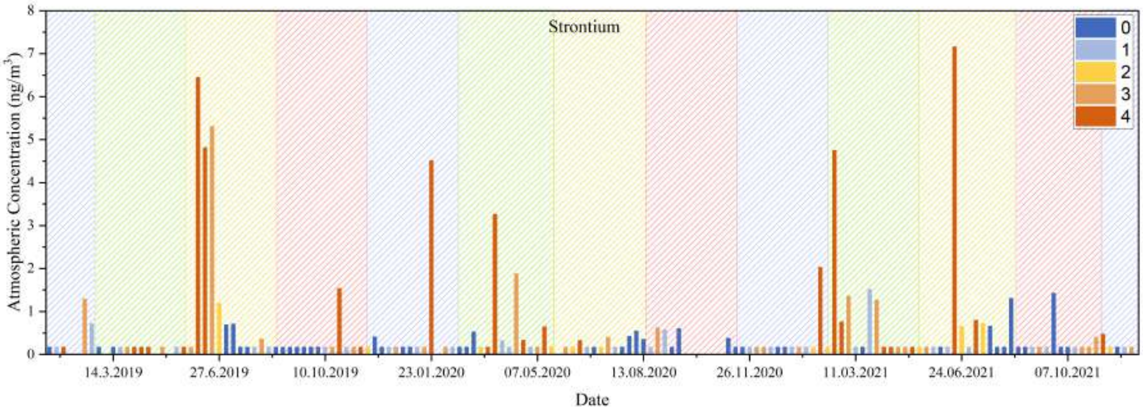

(j) Yearly cycle of Sr, SDEs indicated

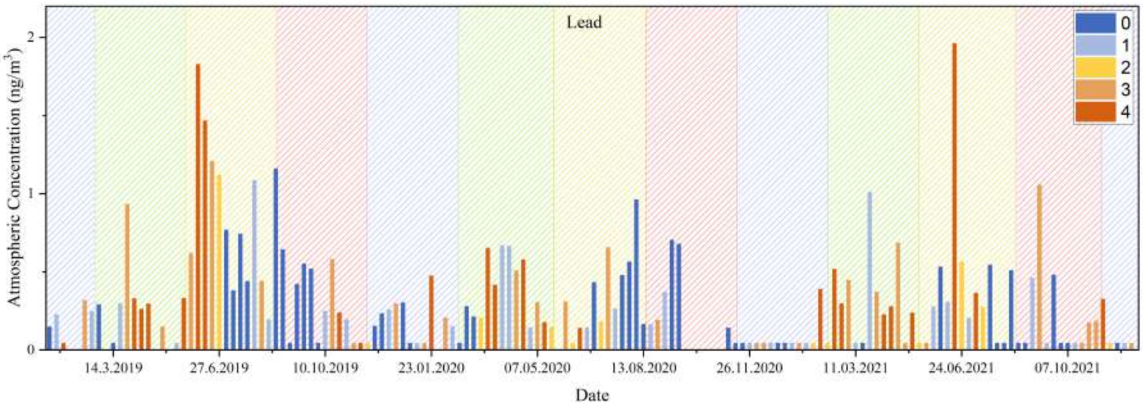

(k) Yearly cycle of Pb, SDEs indicated

Figure 3.14: Time series of elemental concentrations based on weekly samples, with SDE categories indicated, seasons as background (legend for seasons see 3.6)

3.5 Calculation of mineral dust load

To obtain a better idea of the proportion of the mineral dust in the analyzed material, it is not sufficient to consider elemental concentrations. Different formulas using detected elements have been noted in literature to account for the missing weight shares attributed to elements like C, O or H. Thus, a number of these formulas is compared and applied to the data compiled here. Formulas 3.2 - 3.6 were taken from Putaud et al. 2010 [45], 3.7 from Li et al. 2017 [46].

$$MD = 2,9 * Si + 2,1 * Al + 1,4 * Ca + 2,1 * Mg + 1,43 * Fe + 1,55 * K \tag{3.2}$$

$$MD = 2,5 * Si + 2,2 * Al + 1,6 * Ca + 2,4 * Fe + 1,9 * Ti \tag{3.3}$$

$$MD = 7,6 * Al + 2,5 * Ca + 3,5 * Mg + Fe + K \tag{3.4}$$

$$MD = 4,7 * Ca + 3,5 * Mg + Fe + K \tag{3.5}$$

$$MD = 4,5 * Ca^{2+} \tag{3.6}$$

$$MD = (1,41 * Ca + 2,09 * Fe + 1,9 * Al + 2,15 * Si + 1,67 * Ti) * 1,16 \tag{3.7}$$

For the Si/Al ratio, 2,5 is used. Because K could not be measured directly by ICP-MS, available results from IC were used. These formulas were applied to a selection of filters for the calculation of mineral dust, namely the filters that showed the highest sum of identifiable elements with our method applied.

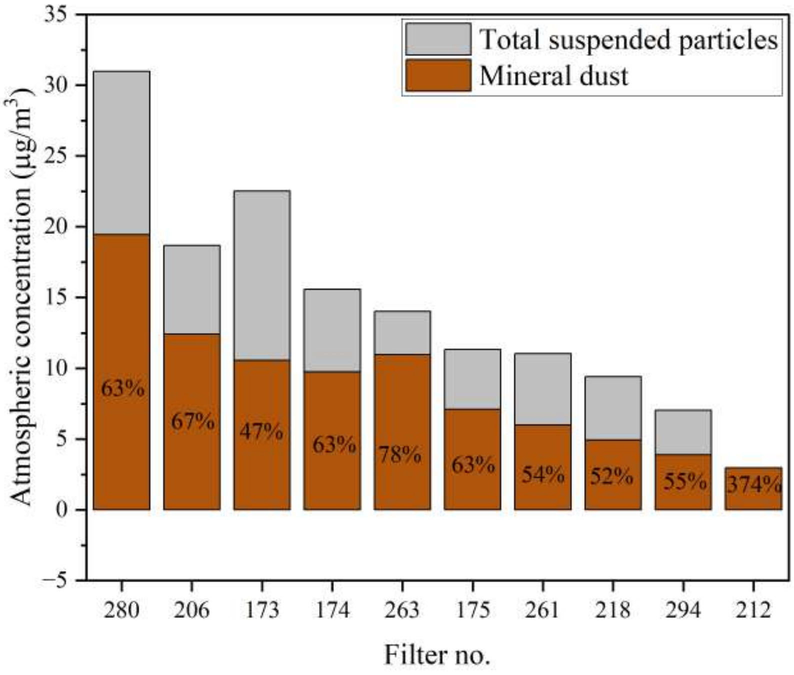

Figure 3.15: Percentage of mineral dust in total suspended matter of highest loaded filters after MD calculation according to Li et al. 2017 [46]

Schauer et al. 2016 [26] report a share of 5 to 80% of the PM mass at SBO consisting of Saharan dust for a period of increased PM occurrence in August 2013, investigated by using values of single scatter albedo wavelength dependence. In fig. 3.15, we want to compare our own results with these numbers by taking the ten highest loaded filters, considering the sum of analytes investigated in this thesis, and comparing it to the associated TSP mass. The findings here suggest values comparable to Schauer et al. 2016 [26], with the highest contribution in the ten highest loaded filters being 78%, not regarding one obvious outlier above 100%. This indicates that using the formula given by Li et al. 2017 [46] gives a relatively good impression of the mineral dust load. To further check the inter-comparability of the different formulas, they were directly contrasted against each other by comparing the results of the ten filters selected as described before.

Looking at the results of correlation analyses presented in table 3.7, comparing results for MD calculations of the ten filters given in fig. 3.15, similarities and differences between the formulas become obvious. A strong impression persists that formula 3.2, 3.3., 3.4 and 3.7 give very similar results, because of their high correlation factors and slopes close to 1. Other formulas, like 3.5 and 3.6, seem to approximate the mineral dust calculations too much, maybe because they leave out elements strongly correlated to SDEs like Al and Fe.

Table 3.7: Comparison of formulas used to approximate the MD load (equations of the linear regression lines and coefficients of correlation)

Formula	3.3 on y-axis	3.4 on y-axis	3.5 on y-axis	3.6 on y-axis	3.7 on y-axis
3.2 on x-axis	$y = 0,9655x - 20,518$ $R^2 = 0,9998$	$y = 0,946x + 33,075$ $R^2 = 0,9964$	$y = 0,499x + 119,68$ $R^2 = 0,8758$	$y = 0,0508x + 1,1358$ $R^2 = 0,817$	$y = 0,969x - 19,84$ $R^2 = 0,9998$
3.3 on x-axis		$y = 0,946x + 33,075$ $R^2 = 0,9964$	$y = 0,5181x + 128,04$ $R^2 = 0,8803$	$y = 0,0526x + 2,071$ $R^2 = 0,8197$	$y = 1,0036x + 0,7325$ $R^2 = 1$
3.4 on x-axis			$y = 0,5374x + 84,702$ $R^2 = 0,9123$	$y = 0,0546x - 2,356$ $R^2 = 0,8499$	$y = 1,0211x - 48,142$ $R^2 = 0,9972$
3.5 on x-axis				$y = 0,1013x - 10,557$ $R^2 = 0,9244$	$y = 1,7062x - 8,2586$ $R^2 = 0,8812$
3.6 on x-axis					$y = 15,633x + 284,33$ $R^2 = 0,8205$

With these considerations in mind, it seems appropriate to use equation 3.7 to approximate the dust concentrations for all filter samples. This was done to evaluate the mineral dust loads related to the previously assigned SDE categories. To find out how mineral dust influences the different categories, the individual dust concentrations of the weeks were averaged and this average then divided by the average TSP mass within each category. We can see in fig. 3.16 that in the first three categories, the mineral dust influence is relatively stable, possibly implying that dust events do not have a strong influence over more than a week. We see that in weeks with SDEs, category 3 and 4, there is an obvious increase in the share of mineral dust compared to total suspended particles, also the more days with a positive diagnosis for SDE over Austria, the bigger the proportion is. Note that this approach is different to calculating the contribution of MD on a single week basis, and averaging these results. This method would give lower concentrations of MD and less differences between the categories, as it is more affected by days with low particulate matter concentrations.

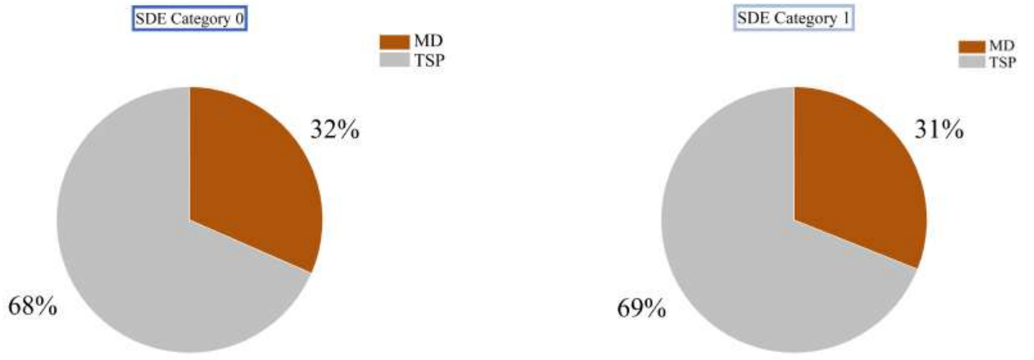

(a) Category 0 (b) Category 1

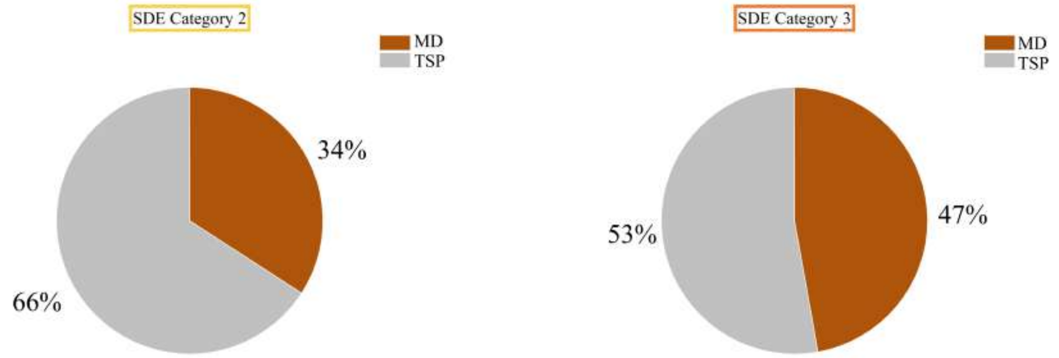

(c) Category 2 (d) Category 3

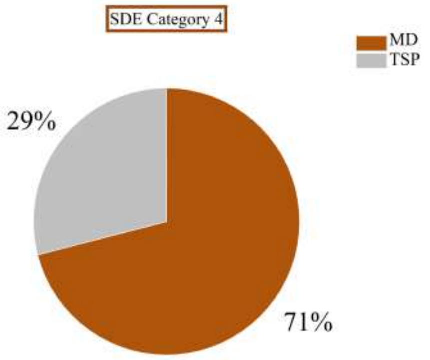

(e) Category 4

Figure 3.16: Percentages of MD in TSP according to SDE categories

Chapter 4

Summary and conclusion

Sahara dust in Europe has been investigated for several decades now, and it has been shown that it has a significant contribution to PM10 levels, especially in southern Europe. The particulate matter transported from North Africa has an impact on ecosystems and the climate. Within this thesis, the Saharan dust in the Eastern Alps has been investigated for occurrence and its chemical composition.

Sampling at Sonnblick Observatory is especially beneficial because of its remote location. In this thesis, samples and data from the years 2019-2021 were processed and evaluated. Data was collected with a β-attenuation monitor and quartz fiber filters, which were analyzed using IC and digestion with subsequent ICP-MS and ICP-OES analyses. In addition, snow samples from March 2022 were evaluated.

For digestion of filters, HBF_4 and HNO_3 were used. The usage of HBF_4 instead of HF promises a safer and, thus, greener alternative, while also eliminating the need for complexing borates after digestion. This method shows good recovery rates for most elements targeted in this thesis. However, it puts a strain on the ICP-MS instrument and further investigation should be considered with ICP-OES systems instead. ICP-OES also shows comparable results for our samples, which indicates that it could be a good alternative for future investigations.

When evaluating the results for temporal trends, we observe annual repetitions. There seem to be higher concentrations in the seasons of spring, summer and fall for most elements. The summers of 2019 and 2021 show especially elevated values, however, this cannot be said for the summer of 2020. Elements associated with Sahara dust show similar patterns in their peak concentrations, indicating a correlation. Around 20% of the average TSP mass could be explained by the elements investigated in this work, with most dominant elements being silicon, aluminium, calcium, iron and magnesium.

When looking at the highest loaded filter collected during an SDE, we can account for more than 40% of elements contained by conducting ICP-MS measurements. Again we see that elements like aluminium, calcium and iron are the most important analyzed metal contributors.

Further evaluations differentiated between days with or without an influence of long range transport of desert dust. For evaluating the amount of SDEs, modelled data provided by ZAMG was used. The finding of 13% of days annually being affected by dust outbreaks is in good accordance with previous surveys. To compare the modelling data with the weekly results of filter sampling, five categories were defined in relation to how close they were to SDEs, or how many days with SD influence were within a week. In the following comparison, we can see that the average atmospheric concentration of elements magnesium, aluminium, calcium, titanium, chromium, manganese, iron, strontium and lead are all highest in the category with the most Sahara dust influx. Elements cobalt and nickel show less of a correlation or no correlation with SDEs. This can be corroborated by looking at single samples of elements in relation to SDE categories. Here, the elements magnesium, aluminium, calcium, titanium, manganese, iron and strontium display most of their higher concentrations in weeks of category 3 or 4.

For the approximation of the mineral dust load, unaccounted mass contributions, such as oxygen, have to be taken into account. Different formulas taken from literature were employed, and a Si/Al ratio of 2,5 (taken from literature and corroborated by XRF measurements) was used. Applying this to the 10 filters with the highest sums of analyzed elements, we see that the share of MD in TSP reaches up to 78% when excluding one probable outlier. When connecting the MD results with the defined categories, we can see that the influence of SDEs in previous or following weeks does not have a very strong effect, but MD share clearly rises with the number of days affected by SD.

List of Figures

List of Tables

Chapter 5

Appendix

Table A1: Atmospheric concentrations of analyzed elements, measured using ICP-MS, N/A: Filter not available

Filter	Date	Atmospheric concentration ICP-MS measurements (ng/m^3)											TSP Sharp Monitor (µg/m^3)	SDE
Number	Start	24 Mg	27 Al	44 Ca	48 Ti	52 Cr	55 Mn	56 Fe	59 Co	61 Ni	86 Sr	208 Pb		Classification
152	17.01.2019	14,5	27,3	26,4	0,872	0,167	0,308	3,03	0,00553	0,163	0,172	0,147	1,64	0
153	24.01.2019	14,5	41,0	26,4	0,872	1,05	0,308	13,7	0,00553	1,07	0,172	0,225	1,23	1
154	31.01.2019	14,5	23,5	26,4	0,872	0,167	0,308	1,77	0,00553	0,163	0,172	0,0429	1,01	4
155	07.02.2019	N/A	N/A	N/A	N/A	N/A	N/A	N/A	N/A	N/A	N/A	N/A	1,69	2
156	N/A	N/A	N/A	N/A	N/A	N/A	N/A	N/A	N/A	N/A	N/A	N/A	N/A	N/A
157	14.2.2019	32,4	426	210	21,0	0,538	3,00	214	0,994	0,304	1,29	0,316	4,14	3
158	21.2.2019	14,5	657	337	18,4	4,69	0,919	91,5	0,0821	2,98	0,713	0,247	2,26	1
159	1.3.2019	14,5	61,2	213	0,872	0,167	0,308	21,5	0,00553	0,437	0,172	0,290	2,85	0
160	7.3.201	N/A	N/A	N/A	N/A	N/A	N/A	N/A	N/A	N/A	N/A	N/A	1,75	0
161	14.3.2019	14,5	24,9	26,4	0,872	0,167	0,308	9,46	0,00553	0,163	0,172	0,0429	1,81	0
162	21.3.2019	14,5	35,9	26,4	0,872	0,167	0,308	18,9	0,00553	0,163	0,172	0,298	2,49	1
163	28.3.2019	14,5	63,9	26,4	1,85	0,167	0,308	36,7	0,00553	0,346	0,172	0,932	5,52	3
164	4.4.2019	14,5	44,8	26,4	0,872	0,167	0,308	8,49	0,590	0,163	0,172	0,327	2,59	4
165	11.4.2019	14,5	42,8	26,4	0,872	0,167	0,308	18,8	0,00553	0,163	0,172	0,261	3,46	4
166	18.4.2019	14,5	92,5	117	4,17	0,167	0,308	47,2	0,00553	0,163	0,172	0,293	3,99	4
167	25.4.2019	N/A	N/A	N/A	N/A	N/A	N/A	N/A	N/A	N/A	N/A	N/A	3,39	4
168	5.5.2019	14,5	83,8	56,4	0,872	0,656	0,308	22,3	0,00553	0,933	0,172	0,149	2,56	3
169	9.5.2019	N/A	N/A	N/A	N/A	N/A	N/A	N/A	N/A	N/A	N/A	N/A	1,41	1
170	16.5.2019	14,5	36,1	26,4	0,872	0,167	0,308	6,38	0,00553	0,332	0,172	0,0429	1,93	1
171	23.5.2019	14,5	51,2	55,7	1,91	0,167	0,308	24,7	0,00553	0,550	0,172	0,331	2,86	4
172	30.5.2019	14,5	94,6	180	4,18	0,167	0,308	50,9	0,00553	0,163	0,172	0,618	4,70	3
173	6.6.2019	276	1250	1680	80,0	1,41	9,77	739	0,245	1,32	6,45	1,83	22,5	4
174	13.6.2019	247	1160	1510	67,8	1,34	9,69	694	0,233	1,11	4,81	1,47	15,6	4

Table A1 continued: Atmospheric concentrations of analyzed elements, measured using ICP-MS, N/A: Filter not available

Filter	Date	Atmospheric concentration ICP-MS measurements (ng/m³)											TSP Sharp Monitor (µg/m³)	SDE
Number	Start	24 Mg	27 Al	44 Ca	48 Ti	52 Cr	55 Mn	56 Fe	59 Co	61 Ni	86 Sr	208 Pb		Classification
175	20.6.2019	185	751	1520	44,7	0,792	5,68	416	0,138	0,800	5,31	1,21	11,3	3
176	27.6.2019	48,5	362	470	21,5	0,504	3,16	213	0,0546	0,574	1,19	1,12	9,42	2
177	4.7.2019	14,5	184	185	9,26	0,559	1,28	101	1,55	0,614	0,692	0,767	5,65	0
178	11/7/2019	14,5	75,5	390	3,43	0,713	1,12	58,0	1,39	0,507	0,708	0,379	3,31	0
179	18/7/2019	14,5	103	233	4,99	0,833	0,898	69,3	0,00553	0,441	0,172	0,741	6,12	0
180	25/7/2019	14,5	117	134	5,59	1,12	0,308	65,0	0,00553	0,430	0,172	0,438	3,79	0
181	1/8/2019	14,5	111	90,9	7,59	0,167	0,308	46,6	0,0337	0,378	0,172	1,08	3,56	1
182	8/8/2019	14,5	281	170	17,8	0,167	1,33	132	0,0244	0,438	0,358	0,440	6,89	3
183	15/8/2019	14,5	53,7	26,4	0,872	0,167	0,308	17,8	0,00553	0,388	0,172	0,193	5,23	1
184	22/8/2019	14,5	109	109	6,19	0,167	0,308	58,9	0,00553	0,611	0,172	1,16	8,96	0
185	29/8/2019	14,5	68,1	26,4	2,84	0,167	0,308	36,8	0,00553	0,163	0,172	0,641	4,65	0
186	6/9/2019	14,5	36,4	26,4	0,872	0,167	0,308	6,36	0,00553	0,562	0,172	0,0429	0,783	0
187	12.09.2019	14,5	163	237	8,12	0,167	0,579	94,4	0,00553	0,490	0,172	0,420	3,73	0
188	19.09.2019	14,5	116	156	5,13	0,167	0,308	54,6	0,00553	0,163	0,172	0,550	0,831	0
189	26.09.2019	14,5	47,1	26,4	0,872	0,167	0,308	21,4	0,00553	0,163	0,172	0,518	2,76	0
190	03.10.2019	14,5	56,1	70,2	1,91	0,167	0,308	13,8	0,00553	0,163	0,172	0,0429	0,773	0
191	10.10.2019	14,5	102	128	7,53	0,167	0,308	36,2	0,00553	0,163	0,172	0,249	2,00	1
192	17.10.2019	14,5	169	282	8,87	0,167	0,308	72,8	0,00553	0,163	0,172	0,579	3,38	3
193	24.10.2019	59,0	582	418	32,7	0,167	3,40	294	0,119	0,444	1,53	0,238	6,83	4
194	31.10.2019	14,5	32,8	26,4	0,872	0,167	0,308	1,77	0,00553	0,307	0,172	0,193	0,936	1
195	07.11.2019	14,5	27,3	26,4	0,872	0,167	0,308	1,77	1,15	0,163	0,172	0,0429	0,732	3
196	14.11.2019	14,5	43,6	26,4	0,872	0,167	0,308	1,77	0,00553	0,432	0,172	0,0429	1,24	4
197	21.11.2019	14,5	35,0	26,4	0,872	0,167	0,308	1,77	0,00553	0,163	0,172	0,0429	1,26	2
198	28.11.2019	14,5	38,0	26,4	0,872	0,167	0,308	3,40	1,24	0,163	0,407	0,153	0,571	0

Table A1 continued: Atmospheric concentrations of analyzed elements, measured using ICP-MS, N/A: Filter not available

Filter	Date	Atmospheric concentration ICP-MS measurements (ng/m^3)											TSP Sharp monitor (µg/m^3)	SDE
Number	Start	24 Mg	27 Al	44 Ca	48 Ti	52 Cr	55 Mn	56 Fe	59 Co	61 Ni	86 Sr	208 Pb		Classification
199	05.12.2019	14,5	42,0	26,4	0,872	0,167	0,308	5,61	0,00553	0,163	0,172	0,232	0,770	0
200	12.12.2019	14,5	45,2	26,4	0,872	0,167	0,308	8,74	0,00553	0,163	0,172	0,258	1,46	1
201	19.12.2019	14,5	72,6	112	1,98	0,167	0,308	38,4	0,00553	0,797	0,172	0,295	0,295	3
202	26.12.2019	14,5	68,8	67,8	2,08	0,167	0,308	66,2	0,00553	0,666	0,172	0,302	0,605	0
203	02.01.2020	14,5	24,7	26,4	0,872	0,167	0,308	101	0,00553	0,163	0,172	0,0429	1,48	0
204	09.01.2020	14,5	7,13	91,9	0,872	0,167	0,308	1,77	0,00553	0,163	0,172	0,0429	0,382	1
205	16.01.2020	14,5	7,13	26,4	0,872	0,167	0,308	1,77	0,00553	0,163	0,172	0,0429	0,369	3
206	23.01.2020	181	1690	1230	112	1,387	15,1	926	0,292	0,163	4,51	0,474	18,7	4
207	30.01.2020	N/A	N/A	N/A	N/A	N/A	N/A	N/A	N/A	N/A	N/A	N/A	1,62	2
208	06.02.2020	14,5	71,9	55,3	4,57	0,167	0,308	34,2	0,00553	0,163	0,172	0,206	1,48	3
209	13.02.2020	14,5	14,8	26,4	0,872	0,167	0,308	4,29	0,00553	0,163	0,172	0,150	0,855	1
210	20.02.2020	14,5	24,6	56,7	2,60	0,167	0,308	5,70	0,00553	0,163	0,172	0,043	1,15	0
211	03.03.2020	14,5	219	221	2,71	4,12	0,308	34,0	0,0296	4,45	0,172	0,279	1,36	0
212	05.03.2020	14,5	122	1370	9,60	0,167	2,37	56,3	0,0354	0,163	0,526	0,211	0,797	0
213	13.03.2020	14,5	30,1	86,1	1,94	0,167	0,308	12,1	0,00553	0,163	0,172	0,203	1,72	2
214	19.03.2020	14,5	111	121	6,97	0,167	0,308	58,2	0,0233	0,163	0,172	0,652	3,99	4
215	26.03.2020	14,5	176	442	10,1	0,167	1,12	97,4	0,0257	0,163	3,26	0,414	5,71	4
216	02.04.2020	14,5	96,0	156	4,47	0,588	1,08	61,6	0,557	0,163	0,319	0,669	4,97	1
217	09.04.2020	14,5	138	421	8,28	0,505	1,94	100	0,0344	0,163	0,172	0,665	7,23	1
218	16.4.2020	131	570	853	30,9	0,633	5,50	331	0,124	0,163	1,88	0,507	9,41	3
219	23.04.2020	14,5	90,8	130	4,50	0,167	1,03	61,6	0,574	0,163	0,328	0,577	5,15	4
220	30.04.2020	14,5	26,6	26,4	0,872	0,167	0,308	14,1	0,00553	0,163	0,172	0,144	1,26	1
221	07.05.2020	14,5	71,6	91,2	4,05	0,167	0,308	41,3	0,00553	0,163	0,172	0,305	4,03	3
222	14.05.2020	14,5	173	298	10,6	0,167	0,888	94,5	0,0364	0,163	0,643	0,175	6,11	4

Table A1 continued: Atmospheric concentrations of analyzed elements, measured using ICP-MS, N/A: Filter not available

Filter	Date	Atmospheric concentration ICP-MS measurements (ng/m^3)											TSP Sharp monitor (µg/m^3)	SDE
Number	Start	24 Mg	27 Al	44 Ca	48 Ti	52 Cr	55 Mn	56 Fe	59 Co	61 Ni	86 Sr	208 Pb		Classification
223	21.05.2020	14,5	33,0	26,4	0,872	0,167	0,308	22,9	0,00553	0,163	0,172	0,146	3,21	2
224	N/A	N/A	N/A	N/A	N/A	N/A	N/A	N/A	N/A	N/A	N/A	N/A	N/A	N/A
225	28.05.2020	14,5	109	26,4	5,77	0,167	0,669	64,4	0,418	0,163	0,172	0,308	4,05	3
226	04.06.2020	14,5	7,13	26,4	0,872	0,167	0,308	1,77	0,791	0,163	0,172	0,0429	0,931	2
227	11.06.2020	14,5	17,4	26,4	0,872	0,167	0,308	7,17	0,936	0,163	0,326	0,140	2,14	4
228	18.06.2020	14,5	14,8	26,4	0,872	1,05	0,308	7,25	0,896	0,163	0,172	0,143	3,30	1
229	25.06.2020	14,5	92,9	67,4	5,10	0,167	0,308	53,7	1,03	0,163	0,172	0,432	5,70	0
230	02.07.2020	14,5	26,8	26,4	0,872	0,167	0,308	20,4	0,879	0,163	0,172	0,182	3,30	2
231	09.07.2020	14,5	94,2	108	8,56	0,167	2,80	110	0,872	0,163	0,399	0,655	5,24	3
232	16.07.2020	14,5	39,9	26,4	2,05	0,510	0,818	27,5	0,930	0,163	0,172	0,263	3,87	1
233	23.07.2020	14,5	80,6	78,2	4,75	0,167	0,781	55,0	0,486	0,163	0,172	0,477	5,77	0
234	30.07.2020	14,5	130	193	7,46	0,167	0,955	74,2	0,698	0,163	0,423	0,563	6,08	0
235	06.08.2020	14,5	152	168	8,69	0,167	2,17	116	0,785	0,163	0,546	0,961	9,24	0
236	13.08.2020	14,5	117	58,3	5,02	0,167	0,611	89,2	1,01	0,163	0,353	0,164	3,10	0
237	20.08.2020	14,5	33,2	43,9	0,872	0,167	0,308	19,9	0,925	0,163	0,172	0,163	3,65	1
238	27.08.2020	14,5	32,1	366	0,872	0,167	0,308	13,9	0,897	0,163	0,626	0,191	3,81	3
239	03.09.2020	14,5	249	121	9,46	0,167	0,308	28,2	1,38	0,163	0,570	0,370	3,09	1
240	10/09/2020	14,5	77,9	117	10,5	1,06	0,721	50,4	1,09	0,163	0,172	0,703	4,50	0
241	17/09/2020	14,5	115	91,1	5,34	0,777	1,16	64,9	1,39	0,397	0,601	0,678	4,80	0
242	N/A	N/A	N/A	N/A	N/A	N/A	N/A	N/A	N/A	N/A	N/A	N/A	0,897	0
243	N/A	N/A	N/A	N/A	N/A	N/A	N/A	N/A	N/A	N/A	N/A	N/A	1,48	0
244	N/A	N/A	N/A	N/A	N/A	N/A	N/A	N/A	N/A	N/A	N/A	N/A	1,40	0
245	N/A	N/A	N/A	N/A	N/A	N/A	N/A	N/A	N/A	N/A	N/A	N/A	2,85	0
246	N/A	N/A	N/A	N/A	N/A	N/A	N/A	N/A	N/A	N/A	N/A	N/A	3,71	0

Table A1 continued: Atmospheric concentrations of analyzed elements, measured using ICP-MS, N/A: Filter not available

Filter	Date	Atmospheric concentration ICP-MS measurements (ng/m^3)											TSP Sharp monitor (µg/m^3)	SDE
Number	Start	24 Mg	27 Al	44 Ca	48 Ti	52 Cr	55 Mn	56 Fe	59 Co	61 Ni	86 Sr	208 Pb		Classification
247	N/A	N/A	N/A	N/A	N/A	N/A	N/A	N/A	N/A	N/A	N/A	N/A	1,71	0
248	05/11/2020	14,5	127	87,5	6,87	2,76	0,771	61,0	0,539	0,163	0,373	0,140	1,81	0
249	12/11/2020	14,5	7,13	26,4	0,872	0,167	0,308	1,77	0,513	0,163	0,172	0,0429	1,18	0
250	19.11.2020	14,5	7,13	26,4	0,872	0,167	0,308	1,77	0,541	0,163	0,172	0,0429	0,923	0
251	26.11.2020	14,5	7,13	26,4	0,872	0,167	0,308	1,77	0,00553	0,163	0,172	0,0429	1,02	1
252	03.12.2020	14,5	7,13	26,4	0,872	0,167	0,308	1,77	0,00553	0,163	0,172	0,0429	0,787	3
253	10.12.2020	14,5	40,6	26,4	0,872	1,32	0,308	5,42	0,00553	0,163	0,172	0,0429	0,841	3
254	17.12.2020	14,5	7,13	26,4	0,872	2,12	0,308	1,77	0,00553	0,163	0,172	0,0429	1,28	1
255	24.12.2020	14,5	7,13	26,4	0,872	0,167	0,308	1,77	0,00553	0,163	0,172	0,0429	1,28	0
256	31.12.2020	14,5	7,13	26,4	0,872	0,167	0,308	1,77	0,00553	0,163	0,172	0,0429	1,36	0
257	07.01.2021	14,5	30,2	26,4	0,872	0,167	0,308	5,65	0,00553	0,163	0,172	0,0429	1,28	1
258	14.01.2021	14,5	7,13	26,4	0,872	1,41	0,308	3,16	0,00553	0,163	0,172	0,0429	1,06	3
259	21.01.2021	14,5	7,13	26,4	0,872	0,167	0,308	1,77	0,00553	0,163	0,172	0,0429	1,46	1
260	28.01.2021	14,5	7,13	26,4	0,872	0,712	0,308	1,77	0,00553	0,163	0,172	0,0429	1,93	2
261	04.02.2021	136	738	863	42,37	3,01	5,93	433	0,148	0,163	2,03	0,389	11,0	4
262	11.02.2021	14,5	24,6	26,4	0,872	0,167	0,308	5,93	0,00553	0,163	0,172	0,0429	1,19	2
263	18.02.2021	199	1570	810	91,2	2,61	12,5	866	0,292	0,163	4,75	0,516	14,0	4
264	25.02.2021	14,5	291	127	17,3	0,167	1,85	161	0,0427	0,678	0,760	0,296	4,42	4
265	04.03.2021	46,2	389	338	23,1	0,457	2,98	206	0,0712	0,163	1,35	0,446	5,83	3
266	11.03.2021	14,5	7,13	26,4	0,872	0,167	0,308	9,56	6,65	0,649	0,172	0,0429	2,12	1
267	18.03.2021	14,5	23,8	26,4	0,872	0,167	0,308	7,72	0,00553	0,163	0,172	0,0429	1,12	0
268	25.03.2021	65,5	334	416	19,8	0,167	3,98	195	1,17	0,163	1,51	1,01	7,03	1
269	01.04.2021	49,8	404	336	24,3	0,167	2,86	220	0,0649	0,163	1,26	0,371	6,06	3
270	08.04.2021	14,5	68,4	61,6	6,70	0,167	0,308	43,8	0,159	0,163	0,172	0,225	3,48	4

Table A1 continued: Atmospheric concentrations of analyzed elements, measured using ICP-MS, N/A: Filter not available

Filter	Date	Atmospheric concentration ICP-MS measurements ($\mathrm{ng/m^3}$)											TSP Sharp monitor ($\mathrm{\mu g/m^3}$)	SDE
Number	Start	24 Mg	27 Al	44 Ca	48 Ti	52 Cr	55 Mn	56 Fe	59 Co	61 Ni	86 Sr	208 Pb		Classification
271	15.04.2021	14,5	24,7	26,4	2,30	0,167	0,308	21,3	0,00553	0,163	0,172	0,278	3,30	4
272	22.04.2021	14,5	67,3	105	4,50	0,167	0,892	54,3	0,182	0,163	0,172	0,685	5,40	3
273	29.04.2021	14,5	7,13	26,4	0,872	0,167	0,308	3,48	0,00553	0,163	0,172	0,0429	2,91	3
274	06.05.2021	14,5	68,9	66,9	4,59	0,167	0,308	40,4	0,0632	0,163	0,172	0,236	3,89	4
275	13.05.2021	14,5	22,9	26,4	0,872	0,167	0,308	4,67	0,00553	0,163	0,172	0,0429	2,18	2
276	21.05.2021	14,5	7,13	26,4	0,872	0,167	0,308	1,77	0,00553	0,163	0,172	0,0429	2,64	3
277	27.05.2021	14,5	33,6	64,4	2,88	0,167	0,308	35,6	0,0315	0,163	0,172	0,277	3,50	1
278	03.06.2021	14,5	27,4	26,4	5,49	0,167	0,308	36,0	0,130	0,163	0,172	0,531	4,76	0
279	10.06.2021	14,5	31,2	95,3	2,66	0,167	0,308	42,9	1,24	0,627	0,172	0,306	3,97	1
280	17.06.2021	494	2420	2650	140	3,42	21,4	1430	0,501	1,61	7,16	1,96	31,0	4
281	24.06.2021	41,2	269	393	16,1	0,167	2,38	157	0,280	0,163	0,648	0,565	6,79	2
282	01.07.2021	14,5	7,13	75,6	0,872	0,167	0,308	16,6	0,00553	0,163	0,172	0,205	4,59	1
283	08.07.2021	40,0	362	272	22,5	0,167	2,53	189	0,0768	0,163	0,795	0,363	7,55	4
284	15.07.2021	14,5	147	368	3,57	0,676	1,40	30,9	0,0923	1,52	0,720	0,273	5,96	2
285	22.07.2021	30,2	224	294	15,3	0,167	2,05	136	0,0508	0,163	0,656	0,544	9,84	0
286	29.07.2021	14,5	17,5	91,9	2,00	0,167	0,308	23,9	0,00553	0,163	0,172	0,0429	3,43	0
287	05.08.2021	14,5	20,5	65,4	0,872	0,167	0,308	19,3	0,282	0,163	0,172	0,0429	5,47	0
288	12.08.2021	72,3	474	422	28,9	1,47	3,87	265	0,104	0,163	1,30	0,509	9,03	0
289	19.08.2021	14,5	22,6	70,4	1,83	0,644	0,308	22,3	0,00553	0,163	0,172	0,0429	3,41	0
290	26.08.2021	14,5	7,13	26,4	0,872	0,167	0,308	1,77	0,0299	0,163	0,172	0,0429	1,02	0
291	02.09.2021	14,5	69,1	86,3	2,95	0,167	0,308	42,6	0,00553	0,330	0,172	0,460	5,09	1
292	09.09.2021	14,5	98,2	146	5,48	0,433	1,25	78,5	0,0272	0,451	0,172	1,06	7,15	3
293	16.09.2021	14,5	7,13	26,4	0,872	0,167	0,308	5,00	0,00553	0,163	0,172	0,0429	1,58	1
294	23.09.2021	70,0	400	916	23,6	1,36	2,86	190	0,0760	1,42	1,42	0,480	7,04	0

Table A1 continued: Atmospheric concentrations of analyzed elements, measured using ICP-MS, N/A: Filter not available

Filter	Date	Atmospheric concentration ICP-MS measurements (ng/m^3)											TSP Sharp monitor (µg/m^3)	SDE
Number	Start	24 Mg	27 Al	44 Ca	48 Ti	52 Cr	55 Mn	56 Fe	59 Co	61 Ni	86 Sr	208 Pb		Classification
295	30.09.2021	14,5	16,4	26,4	0,872	0,167	0,308	4,02	0,00553	0,491	0,172	0,0429	0,511	0
296	07.10.2021	14,5	20,7	26,4	0,872	0,167	0,308	4,85	0,00553	0,163	0,172	0,0429	0,181	0
297	14.10.2021	14,5	34,8	55,4	0,872	0,167	0,308	5,72	0,00553	0,882	0,172	0,0429	0,855	1
298	21.10.2021	14,5	41,7	58,9	1,81	7,81	0,308	57,5	0,00553	5,72	0,172	0,0429	0,243	3
299	28.10.2021	14,5	45,7	81,5	0,872	0,167	0,308	13,9	0,00553	0,363	0,172	0,173	0,076	3
300	04.11.2021	14,5	190	314	12,2	0,701	0,867	89,9	0,0335	1,10	0,398	0,186	3,57	3
301	11.11.2021	14,5	306	268	19,2	0,488	1,64	148	0,0517	1,14	0,469	0,324	4,07	4
302	18.11.2021	14,5	27,1	26,4	0,872	0,167	0,308	1,77	0,00553	0,726	0,172	0,0429	0,992	2
303	25.11.2021	14,5	16,2	26,4	0,872	0,167	0,308	1,77	0,00553	0,741	0,172	0,0429	1,94	0
304	02.12.2021	14,5	23,3	26,4	0,872	0,167	0,308	1,77	0,0243	1,18	0,172	0,0429	2,63	1
305	09.12.2021	14,5	7,13	26,4	0,872	0,167	0,308	1,77	0,00553	0,883	0,172	0,0429	2,19	3

Table A2: Atmospheric concentration of analyzed elements, measured using ICP-OES, N/A: value not available due to negative value

	Atmospheric concentration ICP-OES measurements (ng/m^3)									
Filter	Mg	K	Fe	Mn	Ni	Cr	Ca	Al	Pb	Ti
Number	$\lambda = 279{,}553$	$\lambda = 766{,}49$	$\lambda = 259{,}94$	$\lambda = 293{,}93$	$\lambda = 231{,}604$	$\lambda = 284{,}325$	$\lambda = 393{,}366$	$\lambda = 396{,}152$	$\lambda = 220{,}353$	$\lambda = 334{,}941$
304	104	N/A	15,0	2,18	N/A	3,39	65,0	95,0	22,2	0,979
296	104	29,3	24,5	3,69	N/A	4,96	74,5	92,7	3,79	1,98
282	113	33,8	36,0	2,49	N/A	N/A	103	82,1	N/A	2,06
299	107	16,8	32,1	4,94	N/A	1,18	111	110	5,48	2,44
233	119	46,2	77,2	6,77	N/A	N/A	143	155	5,70	5,26
211	328	64,3	56,2	15,1	5,07	7,35	185	283	4,08	4,24
214	117	74,1	77,1	4,59	4,56	0,669	116	182	N/A	6,92
234	131	78,3	96,3	7,36	N/A	2,38	193	204	2,70	8,11
217	153	108	115	7,26	N/A	2,23	299	204	0,323	8,13
192	119	41,1	77,0	8,06	N/A	1,40	171	201	3,86	6,00
300	133	61,8	104	3,93	0,845	2,89	182	248	N/A	9,79
182	149	104	143	7,67	N/A	2,30	182	354	7,44	13,6
301	140	64,6	145	6,84	N/A	1,16	164	325	N/A	14,2
239	133	44,8	52,0	5,12	N/A	0,767	189	362	16,08	7,69
294	218	128	209	5,88	3,24	2,91	440	444	N/A	18,2
268	196	138	217	7,15	0,856	3,65	371	418	N/A	18,8
176	190	133	232	8,84	2,09	3,03	356	455	N/A	20,7
157	173	109	236	7,95	N/A	2,86	248	507	0,0972	21,9
288	205	164	275	8,71	N/A	1,46	354	547	5,36	24,4
193	194	120	283	8,87	0,866	2,94	289	619	23,1	27,0
218	264	215	333	10,5	1,75	1,44	619	635	N/A	28,9
175	330	255	435	9,10	1,89	0,102	1030	867	N/A	40,2
261	268	247	429	11,0	3,23	3,37	726	851	N/A	39,8

Table A3: Atmospheric concentration of analyzed ions, measured using Ion Chromatography, N/A: Filter not available

Filter	Atmospheric concentration IC measurements (µg/m^3)				Filter	Atmospheric concentration IC measurements (µg/m^3)			
Number	SO_4^{2-}	Mg^{2+}	K^+	Ca^{2+}	Number	SO_4^{2-}	Mg^{2+}	K^+	Ca^{2+}
152	0,369	0,000797	0,00286	0,00141	177	1,024	0,0145	0,0216	0,138
153	0,171	0,000582	0,00599	0,0186	178	0,693	0,0183	0,0179	0,226
154	0,0939	0,00109	0,00190	0,00647	179	1,25	0,0133	0,0304	0,140
155	N/A	N/A	N/A	N/A	180	1,04	0,00647	0,0204	0,0600
156	N/A	N/A	N/A	N/A	181	0,828	0,00462	0,0121	0,0380
157	0,375	0,0116	0,0151	0,183	182	1,02	0,0121	0,0292	0,0913
158	0,234	0,00406	0,0121	0,0590	183	0,864	0,00409	0,0167	0,0250
159	0,232	0,00457	0,0114	0,0228	184	2,97	0,00704	0,0433	0,0574
160	N/A	N/A	N/A	N/A	185	1,77	0,00354	0,0246	0,0266
161	0,177	0,00221	0,00399	0,0149	186	0,246	0,00140	0,00411	0,00635
162	0,276	0,00300	0,00893	0,0286	187	0,482	0,00951	0,0153	0,123
163	0,989	0,00881	0,0334	0,0513	188	0,155	0,00868	0,00772	0,0600
164	0,832	0,00267	0,0106	0,0240	189	0,493	0,00334	0,0128	0,0195
165	0,683	0,00309	0,0176	0,0302	190	0,146	0,00150	0,00285	0,0118
166	0,606	0,00771	0,0153	0,0631	191	0,292	0,00463	0,00752	0,0434
167	0,0224	0,0106	0,0309	0,122	192	0,399	0,0109	0,0102	0,119
168	0,653	0,00619	0,0134	0,0195	193	0,811	0,0208	0,0246	0,206
169	N/A	N/A	N/A	N/A	194	0,0745	0,000271	0,000764	0,00141
170	0,214	0,00161	0,00247	0,00761	195	0,0622	0,000609	0,000774	0,00508
171	0,442	0,00338	0,00890	0,0448	196	0,0526	0,00108	0,000787	0,0197
172	0,675	0,00975	0,0122	0,114	197	0,0811	0,00320	0,0762	0,0156
173	2,69	0,0714	0,0607	0,953	198	0,116	0,000657	0,000761	0,00428
174	1,48	0,0630	0,0499	0,789	199	0,127	0,00107	0,00304	0,00605
175	1,63	0,0435	0,0406	0,966	200	0,143	0,00199	0,00332	0,0110
176	1,15	0,0257	0,0309	0,258	201	0,0416	0,00459	0,00428	0,0627

Table A3 continued: Atmospheric concentration of analyzed ions, measured using Ion Chromatography, N/A: Filter not available

Filter	Atmospheric concentration IC measurements (µg/m³)				Filter	Atmospheric concentration IC measurements (µg/m³)			
Number	SO_4^{2-}	Mg^{2+}	K^+	Ca^{2+}	Number	SO_4^{2-}	Mg^{2+}	K^+	Ca^{2+}
202	0,0922	0,00240	0,00438	0,0393	227	0,272	0,00261	0,00611	0,0116
203	0,0505	0,00100	0,000756	0,0114	228	0,388	0,00381	0,0111	0,0154
204	0,125	0,000677	0,00153	0,00310	229	0,764	0,00915	0,0183	0,0622
205	0,154	0,00106	0,00261	0,00434	230	0,283	0,0113	0,0130	0,0378
206	0,359	0,0478	0,0583	0,448	231	0,638	0,0138	0,0272	0,0882
207	N/A	N/A	N/A	N/A	232	0,520	0,00383	0,0155	0,0353
208	0,140	0,00430	0,00856	0,0290	233	0,742	0,00831	0,0282	0,0742
209	0,122	0,00302	0,00655	0,0301	234	0,607	0,0139	0,0259	0,118
210	0,109	0,00158	0,000757	0,0139	235	1,40	0,0157	0,0547	0,113
211	0,0739	0,00102	0,00255	0,00472	236	0,317	0,00488	0,0132	0,0357
212	0,105	0,0239	0,0166	0,540	237	0,242	0,00700	0,0111	0,0403
213	0,246	0,00282	0,00870	0,0180	238	0,302	0,00387	0,0096	0,0187
214	0,777	0,00716	0,0281	0,0499	239	0,257	0,00758	0,0121	0,0544
215	1,11	0,0256	0,0243	0,197	240	0,535	0,00906	0,0232	0,0875
216	0,761	0,0158	0,0348	0,126	241	0,785	0,00729	0,0306	0,0602
217	1,13	0,0275	0,0463	0,224	242	N/A	N/A	N/A	N/A
218	0,594	0,0430	0,0285	0,511	243	N/A	N/A	N/A	N/A
219	0,766	0,0121	0,0208	0,118	244	N/A	N/A	N/A	N/A
220	0,280	0,00509	0,00681	0,0236	245	N/A	N/A	N/A	N/A
221	0,373	0,00954	0,0125	0,0663	246	N/A	N/A	N/A	N/A
222	0,345	0,0125	0,0105	0,156	247	N/A	N/A	N/A	N/A
223	0,569	0,00699	0,00913	0,0295	248	N/A	N/A	N/A	N/A
224	N/A	N/A	N/A	N/A	249	0,0732	0,000931	0,00452	0,00805
225	0,603	0,00728	0,00941	0,0516	250	0,117	0,000942	0,00920	0,00715
226	0,0987	0,000604	0,000768	0,00142	251	0,111	0,00187	0,00561	0,0119

Table A3 continued: Atmospheric concentration of analyzed ions, measured using Ion Chromatography, N/A: Filter not available

Filter	Atmospheric concentration IC measurements (µg/m^3)				Filter	Atmospheric concentration IC measurements (µg/m^3)			
Number	SO_4^{2-}	Mg^{2+}	K^+	Ca^{2+}	Number	SO_4^{2-}	Mg^{2+}	K^+	Ca^{2+}
252	0,0232	0,000120	0,00551	0,00144	277	0,512	0,0998	0,0154	0,0635
253	0,0593	0,000459	0,00539	0,00956	278	0,754	0,00659	0,0115	0,0459
254	N/A	N/A	N/A	N/A	279	0,675	0,0114	0,0109	0,0641
255	0,0407	0,000680	0,00198	0,00490	280	1,56	0,142	0,0858	1,85
256	0,0401	0,00113	0,00258	0,00145	281	0,964	0,0306	0,0291	0,257
257	0,298	0,00186	0,00317	0,0114	282	0,492	0,00472	0,0169	0,0355
258	0,101	0,00138	0,00486	0,0167	283	0,562	0,0217	0,0347	0,201
259	0,0310	0,000303	0,000786	0,00145	284	0,257	0,0107	0,0422	0,141
260	0,0192	0,000551	0,000790	0,00146	285	1,12	0,0231	0,0552	0,203
261	0,130	0,0304	0,0228	0,505	286	0,391	0,00466	0,0178	0,0266
262	N/A	N/A	N/A	N/A	287	0,597	0,0105	0,0222	0,0422
263	0,385	0,0638	0,0524	0,552	288	0,682	0,0340	0,0372	0,285
264	0,460	0,0108	0,0321	0,0907	289	0,341	0,00426	0,0162	0,0244
265	0,417	0,0200	0,0228	0,225	290	0,109	0,00965	0,00454	0,00787
266	0,167	0,00197	0,0116	0,0124	291	0,469	0,0075	0,0256	0,0544
267	0,285	0,00299	0,00611	0,0167	292	1,17	0,0142	0,0346	0,0859
268	0,734	0,0335	0,0342	0,283	293	0,183	0,00128	0,00529	0,0102
269	0,416	0,0176	0,0166	0,186					
270	0,345	0,0100	0,0105	0,0528					
271	0,575	0,00470	0,0134	0,0227					
272	0,820	0,0151	0,0245	0,0807					
273	0,211	0,00210	0,00332	0,00820					
274	0,317	0,00767	0,00904	0,0690					
275	0,000700	0,000343	0,000889	0,00164					
276	0,137	0,000795	0,000920	0,00170					

Bibliography

[1] Peter Bruckmann et al., "Staub ist überall - Auch in der Luft", in *Chemie über den Wolken*, edited by Reinhard Zellner und Gesellschaft Deutscher Chemiker, Wiley-VCH, Weinheim, chap. 6, 2011, pp. 105–119.

[2] World Health Organization et al., *WHO global air quality guidelines: particulate matter (PM2. 5 and PM10), ozone, nitrogen dioxide, sulfur dioxide and carbon monoxide*, World Health Organization, 2021.

[3] "Bundesgesetz zum Schutz vor Immissionen durch Luftschadstoffe Anlage 1a Immissionsgrenzwerte", , 2023, `https://www.ris.bka.gv.at/GeltendeFassung.wxe?Abfrage=Bundesnormen&Gesetzesnummer=10011027`, last accessed 02.03.2023.

[4] European Union et al., "Directive 2008/50/EC of the European Parliament and of the Council of 21 May 2008 on ambient air quality and cleaner air for Europe", *Official Journal of the European Union*, 2008.

[5] European Union, "Commission staff working paper: Establishing guidelines for demonstration and subtraction of exceedances attributable to natural sources under the Directive 2008/50/EC on ambient air quality and cleaner air for Europe", *SEC(2011)208*, 2011.

[6] Dennis Mooibroek et al., "PM10 Source Apportionment in Five North Western European Cities—Outcome of the Joaquin Project", in *Airborne particulate matter : sources, atmospheric processes and health*, edited by Ronald E. Hester et al., Royal Society of Chemistry, Cambridge, 2016, pp. 264–292.

[7] Dirk Scheuvens and Konrad Kandler, "On composition, morphology, and size distribution of airborne mineral dust", in *Mineral Dust*, Springer Netherlands, Dordrecht, 2014, pp. 15–49.

[8] A Karanasiou, et al., “Health effects from Sahara dust episodes in Europe: literature review and research gaps”, *Environ Int*, 47, 2012, pp. 107–114.

[9] Florian Thevenon, et al., “Characterization of modern and fossil mineral dust transported to high altitude in the western alps: Saharan sources and transport patterns”, *Adv Meteorol*, 2012, 2012, pp. 1–14.

[10] Mary F Glueck and Charles W Stockton, “Reconstruction of the north Atlantic oscillation, 1429-1983”, *Int J Climatol*, 21(12), 2001, pp. 1453–1465.

[11] I Chiapello and C Moulin, “TOMS and METEOSAT satellite records of the variability of Saharan dust transport over the Atlantic during the last two decades (1979-1997)”, *Geophys Res Lett*, 29(8), 2002, pp. 17–1–17–4.

[12] Tim Jickells, et al., “Biogeochemical impacts of dust on the global carbon cycle”, in *Mineral Dust*, Springer Netherlands, Dordrecht, 2014, pp. 359–384.

[13] Joana A Rizzolo, et al., “Soluble iron nutrients in Saharan dust over the central Amazon rainforest”, *Atmospheric Chemistry and Physics*, 17(4), 2017, pp. 2673–2687.

[14] Thomas Peer, et al., “Mineralogical composition and origin of airborne dust in an alpine environment of Hochtor (Hohe Tauern, Austria): Effects on pedogenesis, biological soil crusts, and vascular plant growth”, *Front Earth Sci*, 10, 2022.

[15] Marion Greilinger, et al., “Contribution of saharan dust to ion deposition loads of high alpine snow packs in Austria (1987–2017)”, *Frontiers in Earth Science*, 6, 2018, p. 126.

[16] Dirk Scheuvens, et al., “Bulk composition of northern African dust and its source sediments — A compilation”, *Earth Sci Rev*, 116, 2013, pp. 170–194.

[17] Lothar Schütz and Kenneth A Rahn, “Trace-element concentrations in erodible soils”, *Atmospheric Environment (1967)*, 16(1), 1982, pp. 171–176.

[18] Gilles Bergametti, et al., “African dust observed over Canary Islands: Source-regions identification and transport pattern for some summer situations”, *Journal of Geophysical Research: Atmospheres*, 94(D12), 1989, pp. 14855–14864.

[19] Paola Formenti, et al., “Recent progress in understanding physical and chemical properties of African and Asian mineral dust”, *Atmos Chem Phys*, 11(16), 2011, pp. 8231–8256.

[20] Wancang Zhao, et al., "Hf-Nd isotopic variability in mineral dust from Chinese and Mongolian deserts: implications for sources and dispersal", *Sci Rep*, 4(1), 2014, p. 5837.

[21] X Li, et al., "Dominance of mineral dust in aerosol light-scattering in the North Atlantic trade winds", *Nature*, 380(6573), 1996, pp. 416–419.

[22] James Haywood and Olivier Boucher, "Estimates of the direct and indirect radiative forcing due to tropospheric aerosols: A review", *Rev Geophys*, 38(4), 2000, pp. 513–543.

[23] Eleanor J Highwood and Claire L Ryder, "Radiative Effects of Dust", in *Mineral Dust*, Springer Netherlands, Dordrecht, 2014, pp. 267–286.

[24] Y Fouquart, et al., "Observations of Saharan aerosols: Results of ECLATS field experiment. Part II: Broadband radiative characteristics of the aerosols and vertical radiative flux divergence", *Journal of Applied Meteorology and Climatology*, 26(1), 1987, pp. 38–52.

[25] Christian Effenberger, *Chemische Massenbilanz der PM10-Fraktion am Hohen Sonnblick*, 2008.

[26] Gerhard Schauer, et al., "Increased PM concentrations during a combined wildfire and Saharan dust event observed at high-altitude Sonnblick Observatory, Austria", *Aerosol and Air Quality Research*, 16(3), 2016, pp. 542–554.

[27] Kathrin Baumann-Stanzer, et al., "Evaluation of WRF-chem model forecasts of a prolonged Saharan dust episode over the Eastern alps", *Aerosol Air Qual Res*, 19(6), 2019, pp. 1226–1240.

[28] ZAMG Sonnblick Observatorium, "Sonnblick Observatorium Homepage", , 2018, URL `https://www.sonnblick.net/de/`, last accessed 19 July 2022.

[29] Kenneth Pye, *Aeolian dust and dust deposits*, Elsevier, 2015.

[30] Kritika Shukla, et al., "A Technical Overview on Beta-Attenuation Method for the Monitoring of Particulate Matter in Ambient Air", *Aerosol and Air Quality Research*, 22, p. 220195.

[31] Hubert Hein and Wolfgang Kunze, *Umweltanalytik mit Spektrometrie und Chromatographie: von der Laborgestaltung bis zur Dateninterpretation*, John Wiley & Sons, 2004.

[32] Edson I Müller, et al., "Wet digestion using microwave heating", in *Microwave-Assisted Sample Preparation for Trace Element Analysis*, Elsevier, 2014, pp. 99–142.

[33] Frank Vanhaecke and Patrick Degryse, *Isotopic analysis : fundamentals and applications using ICP-MS*, Weinheim, 2012.

[34] Noriyuki Yamada, "Kinetic energy discrimination in collision/reaction cell ICP-MS: Theoretical review of principles and limitations", *Spectrochimica Acta Part B: Atomic Spectroscopy*, 110, 2015, pp. 31–44.

[35] Luiza GR Albuquerque, et al., "Evaluation of multi-mixtures of acids for the sample preparation of organic soil amendments for multi-element determination by ICP OES", *Communications in Soil Science and Plant Analysis*, 48(18), 2017, pp. 2210–2217.

[36] N V Korsakova, et al., "Analysis of silicate materials using the microwave-assisted sample preparation", *Inorg Mater*, 46(14), 2010, pp. 1513–1517.

[37] Marion Greilinger, et al., "Temporal changes of inorganic ion deposition in the seasonal snow cover for the Austrian Alps (1983–2014)", *Atmospheric Environment*, 132, 2016, pp. 141–152.

[38] Philip J Silva, et al., "Size and chemical characterization of individual particles resulting from biomass burning of local Southern California species", *Environmental Science & Technology*, 33(18), 1999, pp. 3068–3076.

[39] Georg A Grell, et al., "Fully coupled "online" chemistry within the WRF model", *Atmos Environ (1994)*, 39(37), 2005, pp. 6957–6975.

[40] J Pey, et al., "African dust outbreaks over the Mediterranean Basin during 2001-2011: PM 10 concentrations, phenomenology and trends, and its relation with synoptic and mesoscale meteorology.", *Atmospheric Chemistry & Physics Discussions*, 12(10), 2012.

[41] Paola Formenti, et al., "Mapping the physico-chemical properties of mineral dust in western Africa: mineralogical composition", *Atmospheric Chemistry and Physics*, 14(19), 2014, pp. 10663–10686.

[42] Christian M Carrico, et al., "The importance of carbon and mineral dust to seasonal aerosol properties in the Nepal Himalaya", *Atmospheric Environment*, 37(20), 2003, pp. 2811–2824.

[43] Gilles Bergametti, et al., “Seasonal variability of the elemental composition of atmospheric aerosol particles over the northwestern Mediterranean”, *Tellus B: Chemical and Physical Meteorology*, 41(3), 1989, pp. 353–361.

[44] Donald F Gatz and Joseph M Prospero, “A large silicon-aluminum aerosol plume in central Illinois: North African desert dust?”, *Atmospheric Environment*, 30(22), 1996, pp. 3789–3799.

[45] J-P Putaud, et al., “A European aerosol phenomenology–3: Physical and chemical characteristics of particulate matter from 60 rural, urban, and kerbside sites across Europe”, *Atmospheric Environment*, 44(10), 2010, pp. 1308–1320.

[46] Chaoliu Li, et al., “Re-evaluating black carbon in the Himalayas and the Tibetan Plateau: concentrations and deposition”, *Atmospheric Chemistry and Physics*, 17(19), 2017, pp. 11899–11912.